



**HAL**  
open science

# Predictions on the stellar-to-halo mass relation in the dwarf regime using the empirical model for galaxy formation EMERGE

Joseph A. O’Leary, Ulrich P. Steinwandel, Benjamin P. Moster, Nicolas Martin, Thorsten Naab

► **To cite this version:**

Joseph A. O’Leary, Ulrich P. Steinwandel, Benjamin P. Moster, Nicolas Martin, Thorsten Naab. Predictions on the stellar-to-halo mass relation in the dwarf regime using the empirical model for galaxy formation EMERGE. *Monthly Notices of the Royal Astronomical Society*, 2023, 10.1093/mnras/stad166 . insu-03952517

**HAL Id: insu-03952517**

**<https://insu.hal.science/insu-03952517>**

Submitted on 12 Jul 2023

**HAL** is a multi-disciplinary open access archive for the deposit and dissemination of scientific research documents, whether they are published or not. The documents may come from teaching and research institutions in France or abroad, or from public or private research centers.

L’archive ouverte pluridisciplinaire **HAL**, est destinée au dépôt et à la diffusion de documents scientifiques de niveau recherche, publiés ou non, émanant des établissements d’enseignement et de recherche français ou étrangers, des laboratoires publics ou privés.

# Predictions on the stellar-to-halo mass relation in the dwarf regime using the empirical model for galaxy formation EMERGE

Joseph A. O’Leary<sup>1</sup>,<sup>\*</sup> Ulrich P. Steinwandel<sup>2</sup>, Benjamin P. Moster<sup>3</sup>, Nicolas Martin<sup>4</sup> and Thorsten Naab<sup>3</sup>

<sup>1</sup>Universitäts-Sternwarte, Ludwig-Maximilians-Universität München, Scheinerstr. 1, D-81679 München, Germany

<sup>2</sup>Center for Computational Astrophysics, Flatiron Institute, 162 5th Avenue, New York, NY 10010, USA

<sup>3</sup>Max-Planck Institut für Astrophysik, Karl-Schwarzschild Straße 1, D-85748 Garching, Germany

<sup>4</sup>Observatoire Astronomique de Strasbourg, Université de Strasbourg, 11 rue de l’Université, F-67000 Strasbourg, France

Accepted 2023 January 3. Received 2022 December 10; in original form 2022 May 2

## ABSTRACT

One of the primary goals when studying galaxy formation is to understand how the luminous component of the Universe, galaxies, relate to the growth of structure which is dominated by the gravitational collapse of dark matter haloes. The stellar-to-halo mass relation probes how galaxies occupy dark matter haloes and what that entails for their star formation history. We deliver the first self-consistent empirical model that can place constraints on the stellar-to-halo mass relation down to  $\log_{10}(m^*/M_{\odot}) \leq 5.0$  by fitting our model directly to Local Group dwarf data. This is accomplished by penalizing galaxy growth in late-forming, low-mass haloes by mimicking the effects of reionization. This process serves to regulate the number density of galaxies by altering the scatter in halo peak mass  $M_h^{\text{peak}}$  at fixed stellar mass, creating a tighter scatter than would otherwise exist without a high- $z$  quenching mechanism. Our results indicate that the previously established double-power law stellar-to-halo mass relation can be extended to include galaxies with  $\log_{10}(M_h^{\text{peak}}/M_{\odot}) \gtrsim 10.0$ . Furthermore, we show that haloes with  $\log_{10}(M_h^{\text{peak}}/M_{\odot}) \lesssim 9.3$  by  $z = 4$  are unlikely to host a galaxy with  $\log_{10}(m^*/M_{\odot}) > 5.0$ .

**Key words:** galaxies: abundances – galaxies: dwarf – galaxies: formation – galaxies: haloes – Local Group.

## 1 INTRODUCTION

Galaxy formation in the  $\Lambda$ CDM framework predicts that dwarf galaxies are expected to be the most abundant galaxies in the universe, however, their low luminosities make them particularly difficult to observe in practice. Meanwhile, their sensitivity to feedback processes makes them difficult to model. Additionally, their shallow gravitational potential wells make them not only sensitive to internal feedback processes but also to assumptions on cosmology. Together this makes dwarf galaxies one of the best test-beds for our understanding of both cosmology and the fundamentals of galaxy formation.

Recent advancements in observational techniques have improved both the quantity and quality of dwarf galaxy observations. In particular, these observations have probed to lower magnitudes offering data completeness to lower masses than previously available. Further, follow up measurements have advanced accuracy in measuring the distance (Putman et al. 2021), mass (Woo, Courteau & Dekel 2008) and star formation histories (Weisz et al. 2014, 2019) of these systems. These advancements present the possibility to better compare observations with high resolution theoretical models and open their use as direct constraining data for numerical models.

Most recent theoretical models have focused on utilizing high resolution hydrodynamical zoom-in simulations to explore dwarf

galaxies around the Milky Way (e.g. Sawala et al. 2015, 2016b; Garrison-Kimmel et al. 2019; Fattahi, Navarro & Frenk 2020; Applebaum et al. 2021; Munshi et al. 2021). These approaches simulate large cosmological volumes then re-simulate the Milky Way like haloes at higher resolution. The advantage of zoom simulations in studies of dwarfs is that it provides a large scale cosmological context while providing the resolution necessary to probe low mass satellites in systems similar to the Milky Way, where we have the most observational data. The drawback to this approach is that the SHMR can only be addressed within the context of the Milky Way like haloes and generally does not explore how assumptions made an impact the global SHMR. Furthermore, despite the improved resolution in hydrodynamical zooms, these models are still restricted by uncertain subgrid implementations that could impact the resulting dwarf population.

Despite the fact that direct hydrodynamical zoom simulations are widely adopted in the field as a tool of choice to study dwarf galaxies around the Milky Way, there are some recent notable examples of work that also focused and introduced seminumerical modelling to study dwarf galaxies (e.g. Kravtsov & Manwadkar 2022).

Empirical models offer several distinct advantages over hydrodynamical and semi-analytic models. Because these models operate by relating galaxies to the host halo in post-processing, computational power can instead be devoted to increasing mass resolution without the need to sacrifice statistics by simulating small volumes. And unlike either hydrodynamical simulations or semi-analytic models, empirical models make fewer assumptions on the relevant subgrid

\* E-mail: [joleary@usm.lmu.de](mailto:joleary@usm.lmu.de)

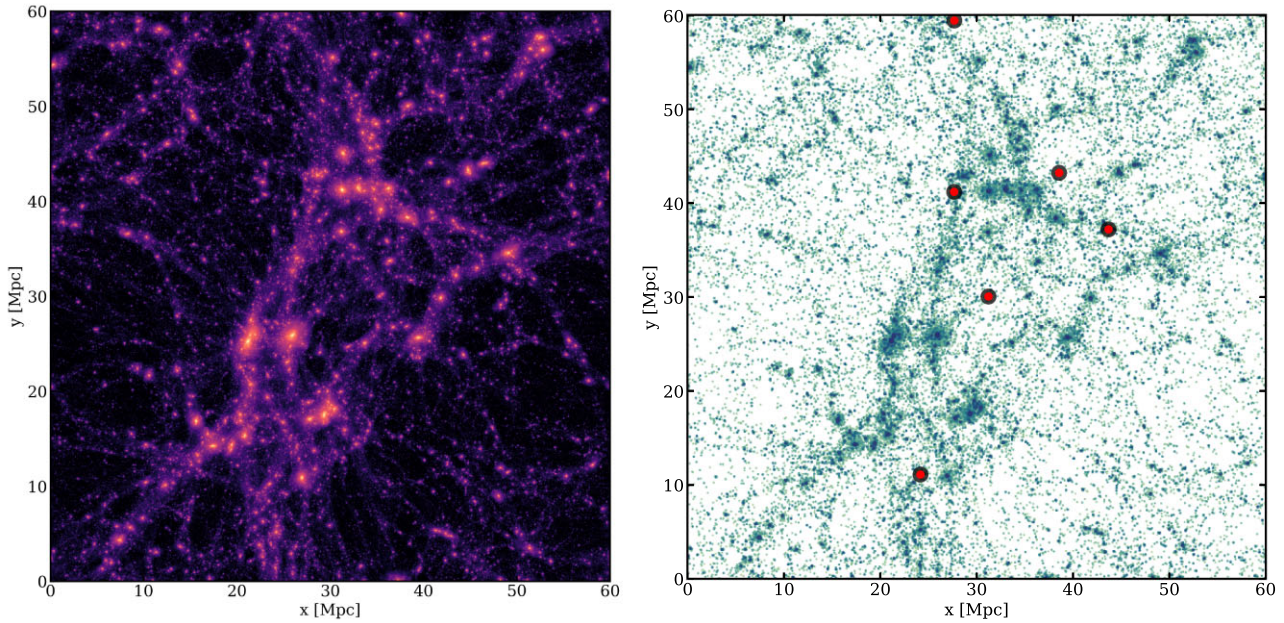


**Figure 1.** On the left, we show the dark matter surface density of our high resolution dark matter simulation with  $2048^3$  particles, specifically designed to capture the smallest dark matter haloes accurately. On the right, we show *all* central galaxies obtained with the empirical model EMERGE. Hereby, we highlight some of the Milky Way analogues in the log stellar mass range between  $10.6$ – $10.78 M_{\odot}$  and the log halo mass range between  $12$ – $12.2 M_{\odot}$ , as black circles with a red face colour.

processes that impact galaxy formation. In this way, the relationship between galaxies and haloes can be explored with less pollution from the personal priors imposed by subgrid models. The big caveat to empirical models is their need for observational data to constrain the model.

The lack of observational data has made empirical approaches to this problem difficult. There have been several recent attempts to quantify the stellar-to-halo mass relation (SHMR) using empirical techniques. Nadler et al. (2019) employed abundance matching on zoom-in simulations tuned to hydrodynamical simulations to make predictions on the abundance of low mass satellites down to  $\log_{10}(m^*/M_{\odot}) \approx 2$ . Meanwhile, using genetic algorithms, Rey & Starkenburg (2022) explore how the merging histories of Milky Way mass hosts affects local dwarf population and statistics. Other recent works (Wang et al. 2021) have taken an exploratory approach by extrapolating the UNIVERSEMACHINE model (Behroozi et al. 2019) into the ultra-faint regime. This is a useful technique to determine where the model must be improved to reproduce the observed characteristics of observed dwarfs. We expand on these approaches by using existing observations to directly constrain our own empirical model EMERGE (Moster, Naab & White 2018).

The goal of this work is to utilize real observables to constrain an empirical model that self consistently relates galaxy properties to dark matter halo properties at dwarf scales. Our aim is to better understand how low mass galaxies populate their haloes, and by doing so, gain a better understanding of their star formation histories. This paper is organized as follows. First, in Section 2.1, we will briefly introduce the  $N$ -body simulations that form the foundation of this work. We discuss the essential functionality and recent updates to the EMERGE model in Section 2.2. Additionally, in Section 2.3, we discuss the new observational data used to constrain our model. In Section 3.1, we introduce the model variations we explore in order to reproduce the observed properties of dwarf galaxies in the local Universe. Section 4 compares

our model implementations with one another, and we discuss the resulting stellar to halo mass relation and star formation histories from our preferred model. Finally, in Section 5, we discuss how our model assumptions might impact our results; in this context, we discuss opportunities for future work and model improvements.

## 2 METHODS, OBSERVATIONS, SIMULATIONS ETC.

### 2.1 N-body simulations

We utilize a cosmological dark matter only  $N$ -body simulation in a periodic box with side lengths of 60 Mpc. This simulation adopts  $\Lambda$ CDM cosmology consistent with (Planck Collaboration 2016) results, where  $\Omega_m = 0.3080$ ,  $\Omega_{\Lambda} = 0.6920$ ,  $\Omega_b = 0.0484$ , where  $H_0 = 67.81 \text{ km s}^{-1} \text{ Mpc}^{-1}$ ,  $n_s = 0.9677$ , and  $\sigma_8 = 0.8149$ . The initial conditions for this simulation were generated using MUSIC (Hahn & Abel 2011) with a power spectrum obtained from CAMB (Lewis, Challinor & Lasenby 2000). The simulation contains  $2048^3$  dark matter particles with particle mass  $9.88 \times 10^5 M_{\odot}$ . The simulation was run from  $z = 124$  to 0 using the Tree-PM code P-GADGET3 (Springel 2005; Beck et al. 2016). In total 147 snapshots were created. Dark matter haloes are identified in each simulation snapshot using the phase space halo finder, ROCKSTAR (Behroozi, Wechsler & Wu 2013a). Halo merger trees are constructed using CONSISTENTTREES (Behroozi et al. 2013b), providing detailed evolution of physical halo properties across time-steps.<sup>1</sup> We show a density projection of the dark matter density in Fig. 1.

<sup>1</sup>Additional information on these simulations, including: configuration files, build info, and parameter files can be found at <https://github.com/jaoleary>.

## 2.2 EMERGE : just the basics

In this section, we provide a short overview of our empirical model EMERGE. This model operates by populating galaxies in simulated dark matter merger trees by directly linking galaxy star formation to the individual growth histories of the host halo. The core of this approach is the baryon conversion efficiency which defines how effectively gas can be converted into stars at some halo mass:

$$\epsilon(M) = 2\epsilon_N \left[ \left( \frac{M}{M_1} \right)^{-\beta} + \left( \frac{M}{M_1} \right)^{\gamma} \right]^{-1}, \quad (1)$$

where  $\epsilon_N$  is the normalization,  $M_1$  is the characteristic halo mass where peak efficiency occurs,  $\beta$  specifies the efficiency slope at masses lower than  $M_1$  and  $\gamma$  is the slope at halo masses larger than  $M_1$ . The parameters are additionally allowed to scale linearly with scale factor such that:

$$\log_{10} M_1(z) = M_0 + M_z \frac{z}{z+1}, \quad (2)$$

$$\epsilon_N = \epsilon_0 + \epsilon_z \frac{z}{z+1}, \quad (3)$$

$$\beta(z) = \beta_0 + \beta_z \frac{z}{z+1}, \quad (4)$$

$$\gamma(z) = \gamma_0. \quad (5)$$

Here, parameters with subscript 0 indicate the  $z = 0$  parameter values and subscript  $z$  indicates the slope of scale factor evolution. The decision to allow parameters to evolve linearly is rather *ad hoc*; that is, there is no particular reason to chose a linear scaling other than its ability to reproduce observed statistics.

For the work described in this paper, we rely on recent improvements to the baryon conversion efficiency model in EMERGE. Other recent works exploring the galaxy-halo connection with neural networks (Moster et al. 2021) have shown that a linear-max scaling for  $\epsilon_N$  can provide an improved fit to observed stellar mass functions (SMFs), especially at intermediate redshift. We have incorporated this proposed change into the version of EMERGE used in this work.

$$\epsilon_N = \begin{cases} \epsilon_0 + \epsilon_z \frac{z}{z+1} & \text{if } \epsilon_N \leq \epsilon_{\text{peak}} \\ \epsilon_{\text{peak}} & \text{otherwise} \end{cases}, \quad (6)$$

Here,  $\epsilon_{\text{peak}}$  is a maximum allowed value for  $\epsilon_N$  and is treated as an additional free parameter in the model.

## 2.3 Observational data

The empirical model is directly constrained by observational data. In addition to the data described in Moster et al. (2018) and O’Leary et al. (2021), we extend the galaxy SMF data down to  $\log_{10}(m^*/M_{\odot}) = 5$  through the inclusion of Local Group dwarf galaxies. In this work, all galaxies within 2 Mpc are defined as members of the Local Group (Putman et al. 2021). We assign a galaxy as a satellite if it is positioned within 300 kpc of either the Milky Way or Andromeda (M31). We construct the SMF using the positively identified dwarf galaxies listed in online data base of McConnachie (2012). Where available, we use galaxy stellar masses from Woo et al. (2008) and a 1.6 mass-to-light ratio otherwise (Bell & de Jong 2001; Martin, de Jong & Rix 2008). We assume 0.8 dex uncertainty in  $\log_{10}(m^*/M_{\odot})$  for each system (Woo et al. 2008).

The dwarf mass function is constructed using 7 bins evenly spaced in  $\log_{10}(m^*/M_{\odot})$ . We then create  $10^4$  random realizations of the locally observed dwarf population by sampling within the mass uncertainty range; each instance is then sampled again, assuming the Poisson error of the distribution. From these random realizations,

we compute the average and  $1\sigma$  interval mass function. Finally, we renormalize the dwarf mass function such that the average value matches the observed average SMF at  $\log_{10}(m^*/M_{\odot}) = 7$ . This requires a vertical adjustment of  $-0.83$  dex to the locally observed SMF. This vertical adjustment is necessary as the global mass function is computed over large volumes and incorporates more void space which lowers the average density compared to our locally measured mass function, which focuses on our own overdense region of the Universe.

Before moving on we should take a moment to consider the implications of relying on Local Group observations to characterize the dwarf galaxies in large volumes. The first clear drawback to this approach is due to the limited sample size. When probing down to  $\log_{10}(m^*/M_{\odot}) = 5$ , observations are at best only complete out to  $\sim 2$  Mpc, this practical limitation restricts our sample of galaxies to 64 confirmed objects. Although extended catalogues exist for dwarf satellites around other hosts and for even lower masses in the Local Group (Geha et al. 2017; Simon 2018; Smercina et al. 2018; Carlsten et al. 2020; Mao et al. 2021), these studies do not offer the completeness we require to constrain our model. This low number of systems results in large error bars on the resulting SMF, which may reduce our ability to make a statistical distinction on the quality of the fit in our proposed model implementations. None the less, we can still make arguments for or against each model variation based on the resulting systems and whether their properties make sense with our current understanding of galaxy growth at low masses. Additionally, an argument could be made that locally observed trends are not representative of the universe at large; however this probes the current limit of our observational capabilities at small scales (see Section 5). Future observations from more sensitive instruments, such as *JWST*, will eventually allow us to explore more systems and build a more complete data set.

## 3 HIGH REDSHIFT QUENCHING

In the discussion of dwarf galaxies there are two particular observational facts we need to contend with. The first is the abundance of dwarf galaxies. The  $\Lambda$ CDM paradigm predicts low mass haloes should appear in the greatest abundances, and recent studies of high redshift star formation indicate that haloes with masses as low as  $M_h \gtrsim 10^5 M_{\odot}$  might be sufficient to initiate star formation (Hirano et al. 2015; Kulkarni, Visbal & Bryan 2021; Schauer et al. 2021). If every low mass halo hosted a bright galaxy, we would expect to observe many thousands of dwarf galaxies in the Local Volume. This prediction conflicts with the relatively low number of dwarf galaxies that have actually been observed and catalogued (McConnachie 2012). The discrepancy between number of observed dwarfs, and the number predicted by  $\Lambda$ CDM is what is known as the missing satellite problem (e.g. Klypin et al. 1999; Moore et al. 1999).

The second complication is in the star formation history (SFH) of these galaxies. Investigation of dwarfs in the Local Group reveals that these galaxies possess low star formation rates and tend to be much older. At the lowest masses observations indicate that for most stars formed by  $z = 6$  (Weisz et al. 2014, 2015). This leaves us with the question: why are dwarf galaxies so old?

One possible solution that can address both is that star formation efficiency is suppressed in low mass haloes at late times due to cosmic reionization. Early work investigating the impact of reionization on the abundance of dwarfs showed that including this feedback process in models for galaxy formation could reconcile the discrepancy of dwarf abundances between  $\Lambda$ CDM predictions and observation (e.g. Efstathiou, Bond & White 1992; Thoul & Weinberg 1996;

**Table 1.** The best fit model parameters for each model variant used in this work. Empty fields indicate the parameter was not left free when fitting that model or was not available in that model. Noted confidence intervals correspond to the  $\pm 1\sigma$  range.

Parameter	Reference	Instantaneous	Lin-max	Logistic
$M_0$	$11.32^{+0.03}_{-0.02}$	-	-	-
$M_z$	$1.45^{+0.06}_{-0.07}$	-	-	-
$\epsilon_0$	$0.02^{+0.01}_{-0.01}$	-	-	-
$\epsilon_z$	$1.70^{+0.01}_{-0.02}$	-	-	-
$\epsilon_{\text{peak}}$	$0.30^{+0.02}_{-0.01}$	-	-	-
$\beta_0$	$2.98^{+0.20}_{-0.22}$	$2.37^{+0.03}_{-0.02}$	$1.89^{+0.04}_{-0.02}$	$2.22^{+0.09}_{-0.05}$
$\beta_z$	$-2.68^{+0.26}_{-0.22}$	$-1.70^{+0.03}_{-0.05}$	$-1.18^{+0.02}_{-0.05}$	$-1.50^{+0.04}_{-0.11}$
$\gamma_0$	$1.25^{+0.01}_{-0.01}$	-	-	-
$f_{\text{esc}}$	$0.59^{+0.02}_{-0.02}$	-	-	-
$f_s$	$0.01^{+0.01}_{-0.01}$	-	-	-
$\tau_0$	$0.81^{+0.10}_{-0.18}$	-	-	-
$\tau_s$	$0.52^{+0.06}_{-0.05}$	$0.40^{+0.01}_{-0.01}$	$0.42^{+0.01}_{-0.01}$	$0.40^{+0.02}_{-0.01}$
$a_q$	-	$0.23^{+0.03}_{-0.02}$	$0.24^{+0.03}_{-0.03}$	$0.19^{+0.03}_{-0.03}$
$M_q$	-	$9.40^{+0.09}_{-0.07}$	$9.34^{+0.05}_{-0.19}$	$9.33^{+0.11}_{-0.08}$
$R_q$	-	-	$1.14^{+0.06}_{-0.06}$	$2.56^{+0.38}_{-0.52}$

Bullock, Kravtsov & Weinberg 2000; Somerville 2002). These models generally predicted that reionization inhibits star formation in haloes with a maximum circular velocity  $V_{\text{peak}} \lesssim 20 \text{ km s}^{-1}$  ( $M_{\text{h}} \lesssim 10^9 M_{\odot}$ ).

In this work, we build on these techniques by incorporating a model for high- $z$  quenching into EMERGE. This model option will complement the already existing mechanisms that impact galaxies in low mass haloes such as environmental quenching and tidal disruption (see Moster et al. 2018; O’Leary et al. 2021, for details).

### 3.1 Model variations

We tested three physically motivated models for a high- $z$  quenching process that impacts low mass haloes. Throughout this work, we compare our results to the “reference” model which is our unaltered EMERGE model with the parameters shown in Table 1. The reference case we show uses the same 60 Mpc box as described in Section 2. However, the parameters used were fit using a lower resolution 200 Mpc box (described in Moster et al. 2018). The Local Group dwarf data were not incorporated into those fits. We also refit the standard EMERGE model with the inclusion of Local Group data as an additional check this variant is simply labelled *Refit*. Additionally, all models were also fit without incorporating the lowest data point in the Local Group SMF, these model results are denoted by a suffix *B* to the model name. This was done to address possible sample incompleteness at the lowest masses.

Our high- $z$  quenching models suppress star formation in low mass-high redshift haloes in a manner consistent with expectations from reionization. The shared characteristic of these methods is that they specify a minimum halo mass  $M_{\text{h}}^{\text{min}}$  required to form stars at some scale factor  $a = 1/(1+z)$ . When a halo does not meet that threshold, its star formation will be set to zero and will remain zero for the remainder of that galaxy’s lifetime. If a halo first appears in the simulation (leaf halo) below the specified threshold, no galaxy will be seeded, and the halo will remain dark (see Section 5.4).

The first and most simple model we test treats the quenching as a uniform, instantaneous process as described by equation (7). Here star formation is shut off in haloes of insufficient mass  $M_q$  by the specified scale factor  $a_q$ . We linearly interpolate halo masses between snapshots to avoid imprinting a preferred quenching scale factor due to time-step discreteness.

$$M_{\text{h}}^{\text{min}}(a) = \begin{cases} M_q & \text{if } a > a_q, \\ 0 & \text{otherwise.} \end{cases} \quad (7)$$

Both of these parameters are free in the model. This model is referred to as *instantaneous* for the remainder of the paper.

Our next model is a linear-max construction given by equation (8). This describes a process where the minimum halo mass needed to form stars increases linearly with increasing scale factor up to some maximum scale factor, after which the halo mass threshold remains constant.

$$M_{\text{h}}^{\text{min}}(a) = \begin{cases} R_q(a - a_q) + M_q & \text{if } a \leq a_q, \\ M_q & \text{otherwise.} \end{cases} \quad (8)$$

Here,  $R_q$  indicates the rate at which the mass threshold increases with scale factor and  $a_q$  indicates the scale factor where the threshold reaches its maximum  $M_q$ . This model is referred to as *lin-max* hereafter.

Finally, we test a logistic model which allows for continuously increasing reionization threshold up to some maximum defined by equation (9).

$$M_{\text{h}}^{\text{min}}(a) = \frac{M_q}{1 + \exp[-R_q(a - a_q)]}, \quad (9)$$

here,  $M_q$  is the maximum threshold mass,  $R_q$  is the transition strength, and  $a_q$  is the mid-point scale factor where the rate reaches its maximum. We implement equation (9) in log-space such that the minimum mass threshold is  $10^0 M_{\odot}$ . Our simulation is of insufficient resolution to probe galaxy formation on those scales, so this floor is somewhat artificial. If the floor value is changed, we could anticipate possible changes in  $R_q$ ,  $a_q$  or both. While this formulation contributes the same number of free parameters as lin-max, the smooth continuous transition delivers a more physically interpretable view of the reionization process while also offering greater flexibility to incorporate additional parameters if needed. This model will be referred as *logistic* for the remainder this work. Furthermore, adopting an evolving threshold mass is consistent with Ricotti, Gnedin & Shull (2008), Rey et al. (2020), Benitez-Llambay & Fumagalli (2021) who employ an evolving UV background during the epoch of reionization.

### 3.2 Fitting

When performing an  $N$ -body simulation, there is typically a trade off between the size of the simulation volume and the particle resolution. Our simulation parameters were chosen to maximize the number of Milky Way like systems while simultaneously providing the resolution necessary to capture the stellar mass to halo mass relation and the associated scatter down to  $\log_{10}(m^*/M_{\odot}) = 5$ . This decision, while necessary for this study, limits which model parameters can be explored in the fitting process largely due to the limited number of more massive systems. Subsequently, we only allow the low mass slope of the baryon conversion efficiency  $\beta_0$ , its redshift evolution  $\beta_z$ , and the stellar mass dependent quenching time-scale  $\tau_s$ , as free parameters in addition to those introduced by our new model variations. All remaining free parameters of the model are fixed to values indicated in Table 1. Additionally, we utilized

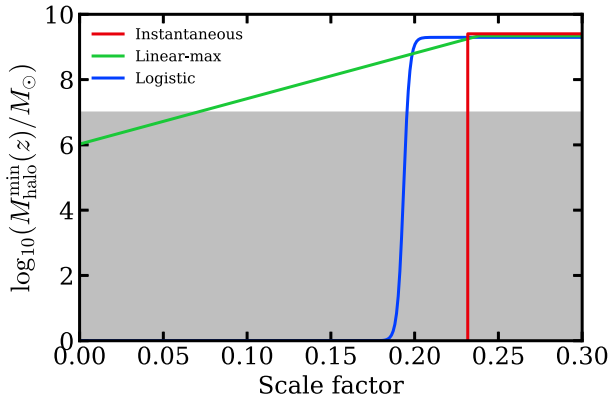


**Figure 2.** The evolution of  $M_h^{\min}(a)$  under our three model variations. Haloes with mass below  $M_h^{\min}(a)$  (coloured lines) have star formation instantaneously quenched. The grey region blocks our sub-resolution halo masses.

binned observational data as opposed to the raw observations as was done in Moster et al. (2018). By fitting to binned data, we minimize the chance of the MCMC getting stuck in a local minimum due to conflicting observations. Finally, we apply a prior to the binned data. This prior applies increased weight to data at low- $z$  and near strong inflection points in order to preserve observed trends where the data is most robustly measured.<sup>2</sup>

## 4 RESULTS

### 4.1 Fits and model selection

Here, we discuss how each model performs in reproducing the range of the observed data, as well as evaluate some evidence based model selection criteria. Table 1 shows the best fit parameters for each model. Empty fields indicate that the parameter is either free or not relevant to the model otherwise the parameters for the reference model have been used. The most notable change to the model parameters is the low mass baryon conversion efficiency slope  $\beta_0$ . With the extended SMF, all models tend to prefer a steeper conversion slope indicating less effective star formation compared to the reference.

Fig. 2 illustrates the evolution of the quenching mass threshold for each best fit model variant. All three of our model variations converge to  $M_q \approx 9.3$ – $9.4$ . With the quenching mass saturating between  $z \approx 3.4$ – $3.75$ . The lin-max and logistic model options, which allow for a time dependent  $M_h^{\min}$ , do not agree on the rate of increase. These models none the less show nearly identical reproduction of the observational data used to constrain EMERGE as well as in the resulting SHMR and star formation histories of dwarfs (see Section 4.2 and Section 4.4, respectively). This likely means there is insufficient data to constrain the time evolution of  $M_h^{\min}$  and that it is not *required* to explore galaxies with  $\log_{10}(m^*/M_\odot) > 5$ .

Fig. 3 shows how each of our models reproduces the  $z = 0$  mass function (coloured lines), compared with the reference (orange line). Each of our model variations successfully reproduces relevant observables, and qualitatively no distinction can be visually identified with respect to the SMF. The lower star formation efficiency in the new models does; however, result in a lower density in the  $7 \leq$

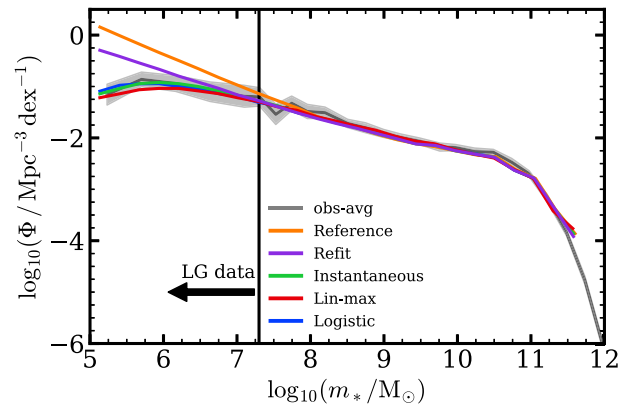


**Figure 3.** A comparison of the global galaxy SMF for our model variations against the observed average SMF. Solid lines illustrate the resulting  $z = 0$  SMF using best fit parameters for each model variant. The grey line and shaded region indicate the observed SMF average from a suite of observational estimates along with the 68 per cent confidence interval. The observed data to the left of the vertical black line illustrates the region where we have extended the observed SMF using the Local Group dwarfs listed in A1.

$\log_{10}(m^*/M_\odot) < 8$  range, but all remain consistent with observed data.

A more quantitative comparison can be performed using an information criterion.<sup>3</sup> This way, we can weight the quality of the fit for each model against the added complexity of additional free parameters. Higher order models can fit the data better, but at some point there will not be enough information to further constrain additional parameters and increasing the order will not provide a better fit to the data. In these schemes models are penalized as additional parameters are added, providing a pathway to selecting the most simple model that can reproduce the data. Table 2 lists the statistical characteristics of each model.

From a statistical point of view, the model lin-max provides the best reproduction of observed data. Beyond these statistical measures, we find very little quantitative differences between each model. For the remainder of this work, we will make all of our comparisons with respect to the logistic model. While the logistic model does not provide any additional predictive power with respect to lin-max, the logistic model provides the greatest flexibility for incorporating new observables, along with the possibility to set a halo mass floor for galaxy formation. Rather than selecting a model which will need to be fundamentally overhauled given new data, it may be preferable to select the model which readily accepts additional parameters to increase its complexity when needed. Ultimately, we found that our conclusions are unaffected by the choice of the high- $z$  quenching model variation we adopt. Furthermore, although refitting the reference with the included Local Group data provides a better fit, we elect to make our comparisons to the unaltered EMERGE parameters. Our comparisons then occupy two extremes to provide a more clear contrast on how the inclusion of this data and high- $z$  quenching impact the SHMR and growth history of dwarfs. Although we will highlight the results from only two models, figures illustrating how each model variant agrees with observed constraints, as

<sup>2</sup>The data used for fitting along with associated weights can be obtained at <https://bitbucket.org/bmoster/emerge>.

<sup>3</sup>Details on these methods are described in the appendix of Moster et al. (2018)

**Table 2.** Model statistics. Models denoted ‘B’ only include data points  $\log_{10}(m_*/M_{\odot}) > 6.0$ .

Model	$\chi^2_{\min}$	$\chi^2_{\text{mean}}$	$N_{\text{p}}$	$p_{\text{D}}$	AIC	BIC	DIC	$-2\ln(Z)$
Refit	906.07	910.69	3	4.62	912.15	923.34	915.31	933.63
Refit_B	790.56	792.88	3	2.32	796.64	807.82	795.20	815.28
Instantaneous	822.38	826.59	5	4.20	832.58	851.16	830.79	858.36
Lin-max	781.83	788.06	6	6.23	794.10	816.37	794.29	828.48
Logistic	827.08	830.00	6	2.93	839.35	861.61	832.93	860.24
Logistic_B	823.02	826.23	6	3.21	835.29	857.53	829.44	846.45

well as predicted relationships and galaxy properties, are shown in B.

#### 4.2 The SMHR

The primary purpose of this work is not to explore the physics of reionization but to better understand how observed dwarfs came to be and how these low mass objects fit into the  $\Lambda$ CDM paradigm. In particular, we are interested in the relationship between dwarf galaxies and their dark matter haloes and the associated scatter in that relationship.

Here, we discuss how the SHMR from our preferred high- $z$  quenching model compares with the reference case. Fig. 4 shows as side by side comparison of these two models in terms of halo peak mass  $\log_{10}(M_{\text{h}}^{\text{peak}}/M_{\odot})$  (blue contours) and present day halo mass  $\log_{10}(M_{\text{h}}^{z=0}/M_{\odot})$  (orange contours). Moster et al. (2010) shows that galaxy stellar mass at any epoch is closely related to the peak halo mass of that galaxy, and the resulting SHMR can be well fit by a double power-law. We can see from the black-solid lines in Fig. 4 that the average SHMR can be well approximated by a power-law relation down to at least  $\log_{10}(M_{\text{h}}^{\text{peak}}/M_{\odot}) \approx 10$ . The results of these models is consistent with an extrapolation of the power-law relation (solid red lines) shown in Moster et al. (2018).

How this relationship evolves for  $\log_{10}(M_{\text{h}}^{\text{peak}}/M_{\odot}) \lesssim 10$  is difficult to ascertain. The reference model produces a relation that extends as a power-law to lower masses. In this case the relationship is primarily determined by the low mass slope of the baryon conversion efficiency. Here, altering the low mass conversion slope can change the slope but the SHMR remains a power-law, by construction. Introducing high- $z$  quenching breaks this relationship by preventing some haloes from forming galaxies in a way that is proportional to the halo growth. This can be clearly seen in the blue contours of the high- $z$  quenching model (right-hand panel) of Fig. 4. Here, we can see a rapid cut off in the SHMR as we approach  $M_{\text{q}}$ . Comparing the blue contours of the reference (left-hand panel) and high- $z$  quenching models we can see that although the models share a similar average SHMR, they diverge strongly in the scatter of  $\log_{10}(M_{\text{h}}^{\text{peak}}/M_{\odot})$  at fixed  $\log_{10}(m_*/M_{\odot})$ . We can conclude that the suppression of the SMF at low masses is primarily due to the elimination of late forming low mass ratio systems,  $m_*/M_{\text{h}}^{\text{peak}}$ , due to a high redshift quenching process.

Previous work has shown that the scatter in the SHMR takes a lognormal distribution at a fixed halo mass (Cooray 2006), similarly we find that our results exhibit this same trend down to  $\log_{10}(M_{\text{h}}^{\text{peak}}/M_{\odot}) \approx 10$ . Due to the lack of observable constraints for  $\log_{10}(m_*/M_{\odot}) < 5$ , we are unable to verify that this trend extends to lower halo masses. Instead, we can compare the scatter in  $\log_{10}(M_{\text{h}}^{\text{peak}}/M_{\odot})$  at fixed stellar mass to better evaluate how high- $z$  quenching impacts scatter compared to the reference treatment.

Fig. 5 illustrates the scatter in halo mass at fixed stellar mass for  $\log_{10}(M_{\text{h}}^{\text{peak}}/M_{\odot})$  (left-hand panel) and  $\log_{10}(M_{\text{h}}^{z=0}/M_{\odot})$  (right-hand

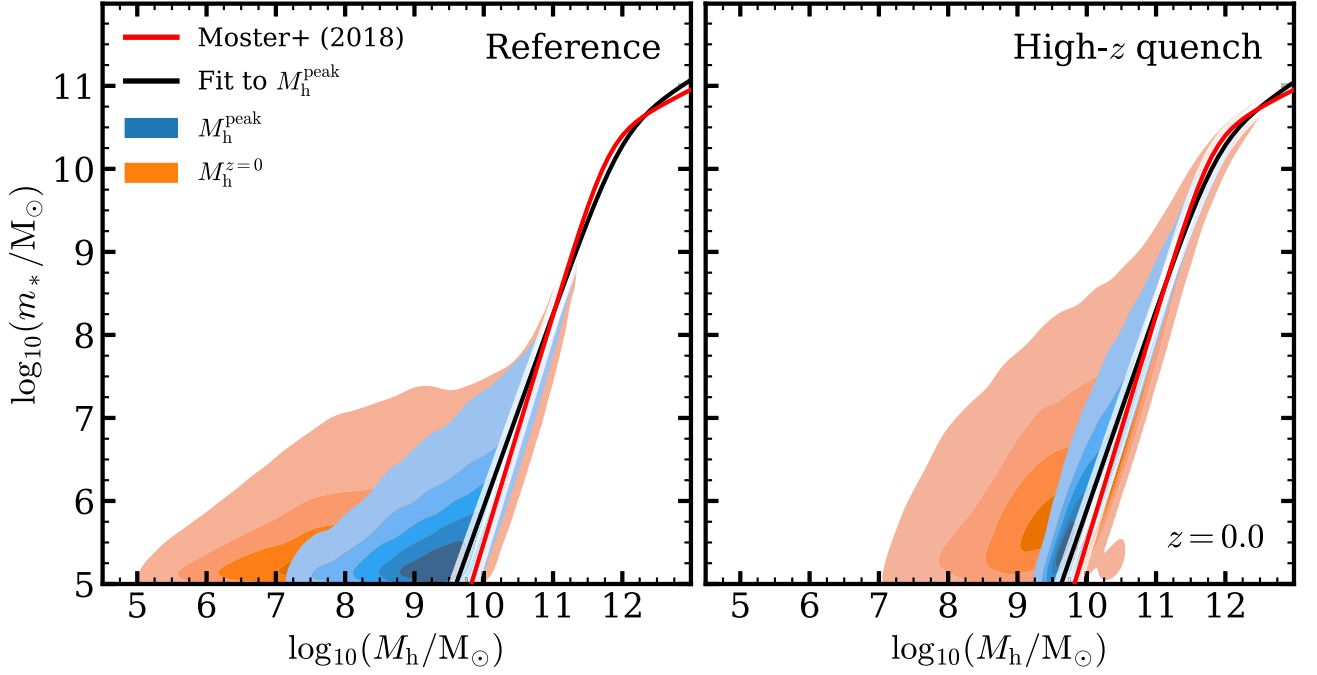
panel). We can see that down to  $\log_{10}(m_*/M_{\odot}) \approx 7$  the distribution in  $\log_{10}(M_{\text{h}}^{\text{peak}}/M_{\odot})$  remains approximately Gaussian with a slight tail extension toward lower masses. For  $\log_{10}(m_*/M_{\odot}) \lesssim 7$ , we find that the standard implementation (dashed lines) produces a highly asymmetric distribution with a pronounced tail toward low halo masses. Conversely, introducing high- $z$  quenching (solid lines) not only reduces the range in scatter but results in a *more* Gaussian distribution. Looking at the same distributions with respect to present day halo mass (right-hand panel), we can see that in the reference model low-mass galaxies occupy a much larger range of halo mass than in the high- $z$  quenching model, this can also clearly be seen in the orange contours of Fig. 4.

Table 3 compares the typical halo mass for a fixed stellar mass interval for each model, measured at the distribution peak along with 68 per cent interval. In general, we find that for the stellar mass ranges evaluated, dwarfs in the high- $z$  quenching model tend to reside in more massive haloes on average compared to the reference model. The difference becomes more pronounced at lower stellar mass, peaking with a 0.15 dex difference for the lowest mass range. Additionally, when evaluating the SHMR using present day halo masses, we should consider the possibility that our formulation for orphan mass loss (O’Leary et al. 2021) may play a role in artificially broadening the distribution if that formulation strips too aggressively. We find that in our reference model orphans contribute between  $\sim 13$  and  $\sim 30$  per cent of the dwarf population  $f_{\text{orph}}$ , while the high- $z$  quenching model tends to produce a lower orphan fraction ranging between  $\sim 10$  and  $\sim 20$  per cent.

Some recent work (Nadler et al. 2019, 2020; Wang et al. 2021) suggests that the singular power-law relation can be extrapolated into the ultra-faint dwarf (UFD) regime for satellites down to  $\log_{10}(m_*/M_{\odot}) \approx 2$ . However, these models have only been constrained down to  $\log_{10}(m_*/M_{\odot}) \approx 8$  and are unable to self consistently reproduce the observed SFH of these systems (see Section 4.4). We find the introduction of high- $z$  quenching substantially alters the SHMR at low masses. In particular, we find these models produce an overabundance of galaxies in the  $\log_{10}(m_*/M_{\odot}) \in [3, 5]$  largely residing in haloes with  $M_{\text{h}}^{\text{peak}} \lesssim M_{\text{q}}$ . This is an obvious consequence of our model which quenches star formation in these haloes but does not disrupt their constituent galaxy, effectively preventing their growth to higher masses along the standard SHMR. Without observables to validate such trends the SHMR should not be extrapolated beyond its range of constraint.

#### 4.3 Satellite populations

Although our models have been fit assuming a global mass function, the majority of observed low mass systems are satellite galaxies of either the Milky Way or Andromeda. In this section, we provide a comparison between the locally observed satellite mass functions and radial distributions compared with simulated systems of similar mass. Our simulated systems are all isolated galaxies (type 0) and



**Figure 4.** The SHMR under the reference model (left-hand panel) compared with the logistic high- $z$  quenching model (right-hand panel). The blue and orange contours show the iso-proportion contours of the SHMR in terms of halo peak mass  $\log_{10}(M_h^{\text{peak}}/M_\odot)$  and present day halo mass  $\log_{10}(M_h^{z=0}/M_\odot)$ , respectively. The solid lines indicate the best fit SHMR assuming a double-power law relation. The black lines show the average relation from the data in this work, while the red lines show the relation from Moster et al. (2018).

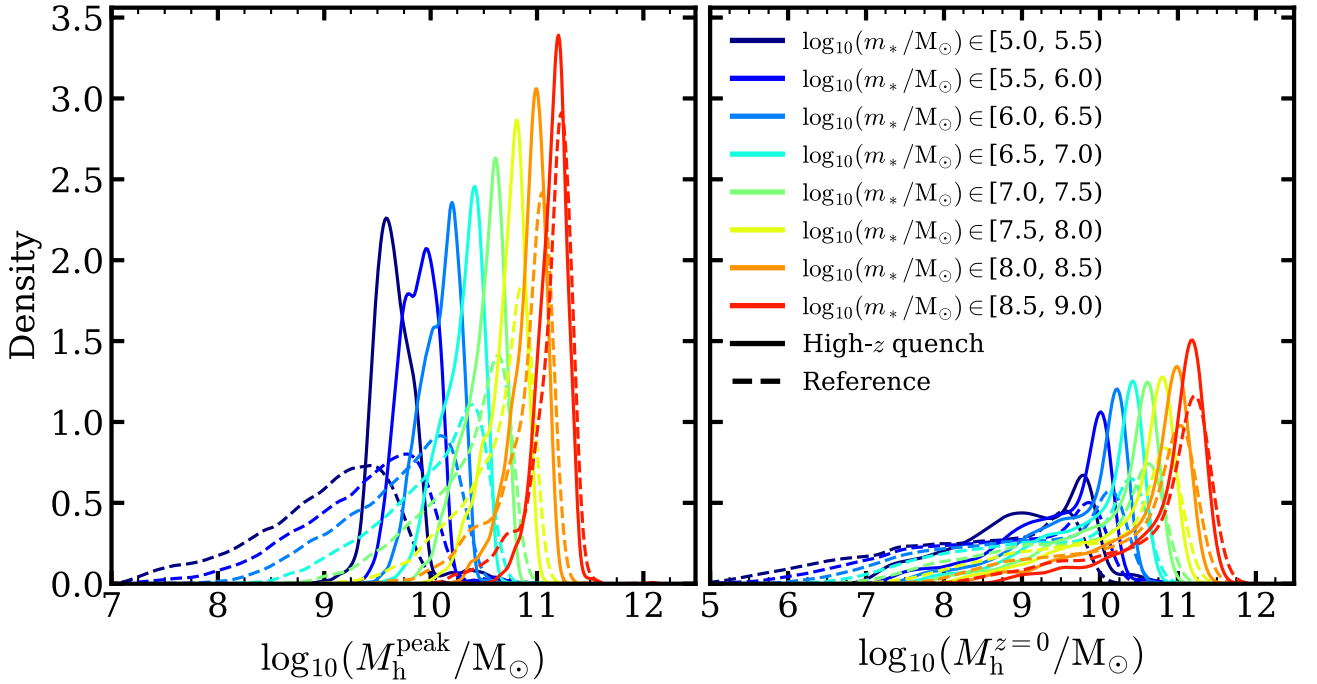


**Figure 5.** The distribution of halo masses at fixed stellar mass. Solid lines correspond to the logistic model and dashed lines are for the reference model. Colours indicate the mass bin for each distribution. The left-hand panel shows distributions in peak halo mass  $\log_{10}(M_h^{\text{peak}}/M_\odot)$  and the right-hand panel shows distributions in present day halo mass  $\log_{10}(M_h^{z=0}/M_\odot)$ .

**Table 3.** Typical halo peak ( $M_h^{\text{peak}}$ ) and current ( $M_h^{z=0}$ ) mass for a range of stellar mass intervals in each model. Masses are measured at the distribution peak with 68 per cent interval measured at iso-density levels.  $N_{\text{gal}}$  shows the number of galaxies in each mass band and  $f_{\text{orph}}$  indicates the fraction of those galaxies that are orphans. All mass values are expressed in  $\log_{10}(m/M_{\odot})$  units.

$m_*$	Reference				High- $z$ quench			
	$N_{\text{gal}}$	$f_{\text{orph}}$	$M_h^{\text{peak}}$	$M_h^{z=0}$	$N_{\text{gal}}$	$f_{\text{orph}}$	$M_h^{\text{peak}}$	$M_h^{z=0}$
$\in [5.0, 5.5)$	133160	0.31	$9.44^{+0.32}_{-0.82}$	$9.55^{+0.28}_{-2.07}$	9950	0.20	$9.58^{+0.23}_{-0.14}$	$9.78^{+0.22}_{-1.31}$
$\in [5.5, 6.0)$	65613	0.26	$9.77^{+0.28}_{-0.79}$	$9.85^{+0.28}_{-2.03}$	12248	0.14	$9.96^{+0.13}_{-0.24}$	$10.01^{+0.22}_{-0.98}$
$\in [6.0, 6.5)$	32929	0.22	$10.09^{+0.24}_{-0.74}$	$10.13^{+0.29}_{-1.93}$	10701	0.12	$10.20^{+0.12}_{-0.26}$	$10.21^{+0.22}_{-0.90}$
$\in [6.5, 7.0)$	16459	0.21	$10.39^{+0.19}_{-0.66}$	$10.40^{+0.30}_{-1.75}$	8033	0.12	$10.41^{+0.13}_{-0.26}$	$10.42^{+0.23}_{-0.94}$
$\in [7.0, 7.5)$	8473	0.19	$10.63^{+0.18}_{-0.54}$	$10.62^{+0.31}_{-1.63}$	5626	0.12	$10.61^{+0.13}_{-0.23}$	$10.61^{+0.25}_{-0.82}$
$\in [7.5, 8.0)$	4515	0.19	$10.85^{+0.16}_{-0.42}$	$10.84^{+0.34}_{-1.41}$	3688	0.13	$10.81^{+0.13}_{-0.20}$	$10.80^{+0.27}_{-0.71}$
$\in [8.0, 8.5)$	2428	0.17	$11.05^{+0.15}_{-0.27}$	$11.03^{+0.37}_{-1.03}$	2398	0.12	$10.99^{+0.13}_{-0.17}$	$10.98^{+0.29}_{-0.62}$
$\in [8.5, 9.0)$	1496	0.13	$11.23^{+0.14}_{-0.18}$	$11.22^{+0.35}_{-0.68}$	1619	0.10	$11.20^{+0.10}_{-0.16}$	$11.18^{+0.26}_{-0.44}$

**Table 4.** Observational estimates of Milky Way and Andromeda stellar and halo masses. Milky Way stellar and halo mass estimates are from Bland-Hawthorn & Gerhard (2016). Andromeda stellar and halo mass estimates are from Sick et al. (2015) and Diaz et al. (2014), respectively.

Name	$m_*$	$M_h^{\text{obs}}$	$M_h^{\text{sim}}$
Milky Way	$10.70^{+0.08}_{-0.10}$	$12.11^{+0.09}_{-0.11}$	$12.43^{+0.27}_{-0.31}$
Andromeda	$11.01^{+0.09}_{-0.08}$	$12.23^{+0.07}_{-0.08}$	$12.86^{+0.27}_{-0.29}$

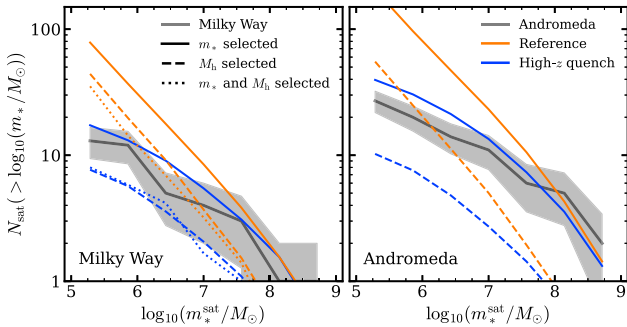


**Figure 6.** Cumulative satellite SMF for satellites with  $5 \leq \log_{10}(m^*/M_{\odot}) < 9$  around Milky Way (left-hand panel) and Andromeda (right-hand panel) like hosts. The grey line and shaded region shows the observed SMFs with Poisson error about the number count in each mass bin. Line colour indicates whether the mass function was generated from the reference model (orange) or the high- $z$  quenching model (blue). Solid lines show the mass function when selecting hosts based on stellar mass, dashed lines by halo mass, and dotted lines by both stellar and halo mass.

selected based on both stellar and halo mass. When searching for simulated Milky Way and Andromeda analogues, we use the stellar and halo mass ranges noted in Table 4.

Fig. 6 shows the cumulative satellite mass function for the Milky Way (left-hand panel) and Andromeda (right-hand panel) under three different host selection criteria. In the first case, we select simulated hosts based on stellar mass only (solid lines). Here, we find that the reference model significantly over predicts the number of satellites for both Milky Way and Andromeda analogues. Enabling high- $z$  quenching substantially improves agreement with observation, exhibiting only a mild over prediction of abundances for satellites  $\log_{10}(m^*/M_{\odot}) \leq 7.0$  around Andromeda analogues. In the second case, we select simulated hosts based on halo mass (dashed lines).

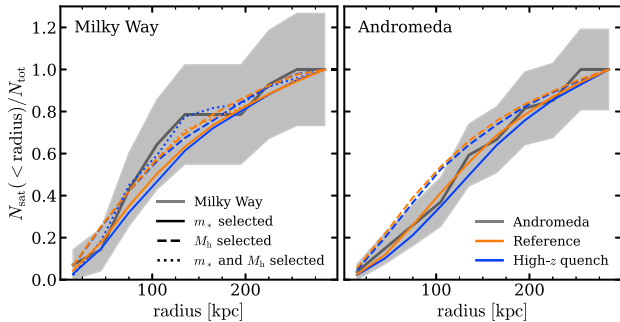
With respect to the Milky Way, the reference model is consistent with observation for  $\log_{10}(m^*/M_{\odot}) \gtrsim 7.0$  with a significant over prediction of satellite abundances at lower masses. Although halo mass selection does improve overall the normalization compared with observations, there is a much steeper slope which drives the over abundances at the lowest masses. Meanwhile, the high- $z$  quenching model reproduces the general trend of the observed SMF but tends to undercut at all masses compared to the observed data. In the case of comparison to Andromeda, we find that selecting hosts based on halo mass under predicts the abundances of satellites in both the reference case and high- $z$  quenching case. Finally, we check the case where we select hosts based on both stellar mass and halo mass. For the Milky Way, we find that selecting based on both mass measures produces a mass function very similar to the halo mass only case. For Andromeda like systems, we are unable to locate any simulated systems that meet both the stellar mass *and* halo mass estimates from observation. In general, our simulated analogues (for both the Milky Way and Andromeda) reside in more massive haloes on average. Table 4 shows the average simulated halo masses where we can see there is no overlap in the observed and simulated halo ranges for Andromeda analogues. The implications of this mismatch are discussed in Section 5.2.

Fig. 7 illustrates the cumulative satellite distribution around Milky Way (left-hand panel) and Andromeda (right-hand panel) like hosts. Here, we find that when selecting hosts based on stellar mass both the reference and high- $z$  quenching model produce a satellite distribution in agreement with observation. For Milky Way analogues, even selecting based on halo mass continues to produce a satellite distribution in line with observed trends. For Andromeda analogues, we find that selecting based on halo mass tends to produce a slightly more centrally concentrated satellite distribution. This could, of course, be driven by the large mismatch in the simulated versus observed halo masses for these analogues.

#### 4.4 SFH

In this section, we evaluate the SFH of low mass systems in this model. We trace back the main branches of the  $z = 0$  galaxy population and compute the average SFH, and stellar mass build up in discrete mass bins.

The top row panel of Fig. 8 compares the SFH of the reference EMERGE model (orange lines) with that of our high- $z$  quenching model (blue lines). Both models share some qualitative similarities. In both model variants, we see that less massive systems experience peak SFR at higher redshift. For equivalent mass ranges, the reference



**Figure 7.** Normalized cumulative radial distribution of satellites with  $5 \leq \log_{10}(m^*/M_{\odot}) < 9$  within 300 kpc of Milky Way (left-hand panel) and Andromeda (right-hand panel) like hosts. The grey line and shaded region shows the observed radial distribution of satellites with Poisson error about the number count in each mass bin. Line colour indicates whether the sample was generated from the reference model (orange) or the logistic model (blue). Solid lines show the distribution when selecting hosts based on stellar mass, dashed lines by halo mass, and dotted lines by both stellar and halo mass. Each line is normalized by the total number of satellites identified in the specified mass and radial ranges.

model experiences peak SFR earlier than the high- $z$  quenching model. For the two most massive bins, the reference case also exhibits a higher peak SFR, for the lowest mass range the high- $z$  quenching model has a higher peak SFR. Further, we can see that in the case of high- $z$  quenching, peak SFR tends to occur very near to the redshift where  $M_q^{\text{peak}}$  is reached.

The bottom panels on Fig. 8 illustrates the cumulative SFH as a fraction of the  $z = 0$  stellar mass for the same sample of simulated galaxies as in the top panel. Although lowest mass systems in the reference model experience their peak SFR at higher redshift than the high- $z$  quenching model, we find that low mass systems in the high- $z$  quenching model are built up more rapidly than in the standard model. However, we find that both models are largely consistent with the observed average SFH determined by Weisz et al. (2014) (grey lines and shaded region).

Another, perhaps more revealing measure of galaxy growth is the formation time. As a galaxy does not form in an instant, we instead attribute the formation time as the 90 per cent formation time-scale  $\tau_{90}$ . This value specifies the cosmological time when a galaxy reached 90 per cent of its present day mass. Fig. 9 compares the formation time of Milky Way and Andromeda satellites (grey points), with the satellite populations around our simulated analogues. In the first panel, we can see that the reference case in general produces a mean formation time that is too long compared with observations, while also failing to reproduce the diversity of formation times seen in the data. The coloured lines indicated the iso-proportion contours for the formation time of galaxies in our simulations. Particularly in the case of the reference model, we can see that EMERGE produces a strongly bi-modal distribution of formation times at low masses. As previously stated, galaxy mass can be directly linked with its associated peak halo mass  $M_h^{\text{peak}}$ . In Fig. 9, we separate the galaxy sample to distinguish whether a galaxy formed before or after  $M_h^{\text{peak}}$ . The blue contours indicate systems that formed after the halo reached  $M_h^{\text{peak}}$  and the red contours show galaxies that formed prior to  $M_h^{\text{peak}}$ . The reference case shows that a majority of low mass systems are formed at late times after halo peak mass indicating that these objects experience significant stellar growth, coasting on their remaining cold gas reservoir, even while their host halo is no longer gaining mass. When high- $z$  quenching is enabled, we can see that

although the majority of galaxies still reach  $\tau_{90}$  after peak mass, a significant portion of these systems form at much earlier times with a mean formation time in much better agreement with observed data. Furthermore, we can see that enabling high- $z$  quenching better reproduces the diversity of formation times seen in local satellites. That these low mass galaxies primarily form after  $M_h^{\text{peak}}$  but at early times, indicates that the majority of these systems have their star formation shut off during their coasting phase as opposed to active build up.

The consequences of these early formation times and premature quenching should therefore be observable in the present day star forming properties of our simulated galaxies. Fig. 10 shows the  $z = 0$  quenched fractions as a function of mass between our two model options. Although quenched fractions are not constrained for  $\log_{10}(m^*/M_{\odot}) < 8.5$ , there are still observed trends at low masses that we should consider. Unsurprisingly, both models exhibit nearly identical quenched fractions in the range used to constrain the model. For dwarf galaxies, we see that the reference model possess a higher quenched fraction than the high- $z$  quenching model for  $6 \lesssim \log_{10}(m^*/M_{\odot}) \lesssim 8.0$ . Toward lower masses, the reference model starts to saturate at near 50 percent quenched. Conversely, the high- $z$  quenching model shows a rapidly increasing quenched fraction toward low masses, nearing 100 percent quenched by  $\log_{10}(m^*/M_{\odot}) = 5$ .

## 5 DISCUSSION AND CONCLUSIONS

### 5.1 Halo mass threshold for galaxy formation

Our model suggests that there should be very few galaxies  $\log_{10}(m^*/M_{\odot}) \gtrsim 5$  with  $\log_{10}(M_h^{\text{peak}}/M_{\odot}) \lesssim 9$  which is in agreement with other theoretical models that show high- $z$  quenching becomes important for haloes  $\log_{10}(M_h^{\text{peak}}/M_{\odot}) \lesssim 9 - 10$  (Thoul & Weinberg 1996; Bullock et al. 2000; Somerville 2002; Kuhlen, Madau & Krumholz 2013; Sawala et al. 2015; Nadler et al. 2019). Our model differs from other empirical models that include high- $z$  quenching in that we do not enforce that all haloes below some threshold should remain dark. The quenching mechanism we implement suppresses star formation as a function of halo mass and time, effectively penalizing star formation in late forming haloes. Recent hydrodynamical models indicate that this distinction may be necessary in order to reproduce the properties of the UFD galaxies with  $\log_{10}(m^*/M_{\odot}) \lesssim 5$  (Garrison-Kimmel et al. 2019; Applebaum et al. 2021; Munshi et al. 2021). Additionally, using high resolution hydrodynamical simulations Schauer et al. (2021) suggest that a minimum halo mass between  $10^6 \sim 10^7 M_{\odot}$  is required to begin star formation, depending on free streaming velocities and the strength of the Lyman–Werner Background. With respect to our work, that would indicate that whatever UFDs exist were likely strongly impacted by a high- $z$  quenching process and reside in haloes with a halo peak mass spanning only  $\sim 2$  orders of magnitude.

### 5.2 Is the Local Group representative?

The work presented so far has assumed that the Local Group is somewhat average with a local mass function that is representative of larger volumes. However, we have so far not provided any quantitative analysis of how ‘normal’ the Local Group is. Fig. 11 shows how the distribution in local SMF slope relates to the vertical offset (in dex) from the global average for stellar mass selected Milky Way analogues. The local slope is defined by the power-law index

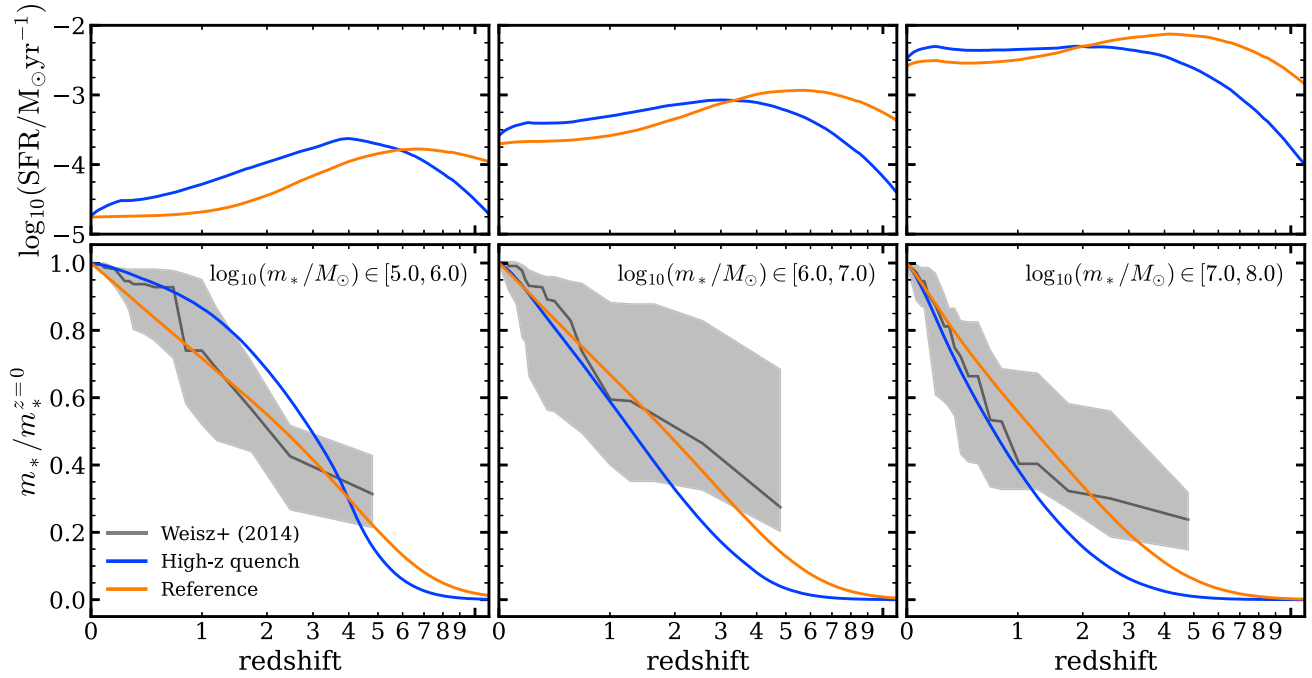


**Figure 8.** SFH in galaxies over time under the reference model (orange panels) and high- $z$  quenching model (blue panels) in three mass intervals. Upper panels show the average star formation rate as a function of redshift. Lower panels show the average cumulative mass growth for the same sample of galaxies. Grey lines illustrate the observed SFH and 68 per cent confidence interval for local dwarfs as computed by Weisz et al. (2014).

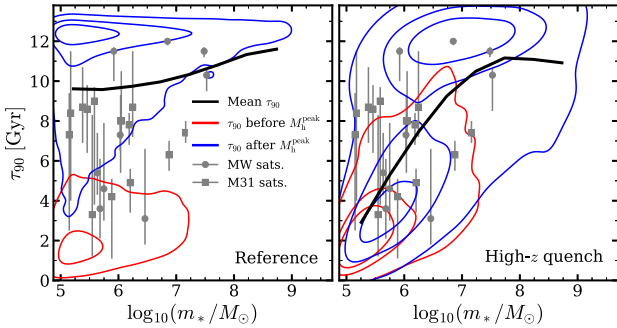


**Figure 9.** The 90 percent formation time-scale  $\tau_{90}$ , red contours indicated galaxies where the formation time-scale occurred before halo peak mass. Blue contours show systems where formation occurred after peak halo mass. Black lines show the average formation time-scale for all systems. Grey points show the formation time-scale for individual observed dwarf satellites (see Table A1).

measured in a 2 Mpc sphere around each analogue. Solid points indicate Milky Way like systems that *also* host one Andromeda like companion within 1 Mpc. The locally measured slope and offset derived from the data in Table A1 is indicated by the red point. If our reference model (orange contours/points) is correct, it would indicate that our locally observed SMF slope is a substantial outlier compared to simulated Milky Way analogues. However, the locally observed offset from the global SMF is average with respect to simulated systems. Additionally, we can see that the simulated systems that host an Andromeda companion are more likely to reside closer to the global slope than those without.

What is possibly more interesting is that even after fitting our model to Local Group data (blue contours/points), we find that

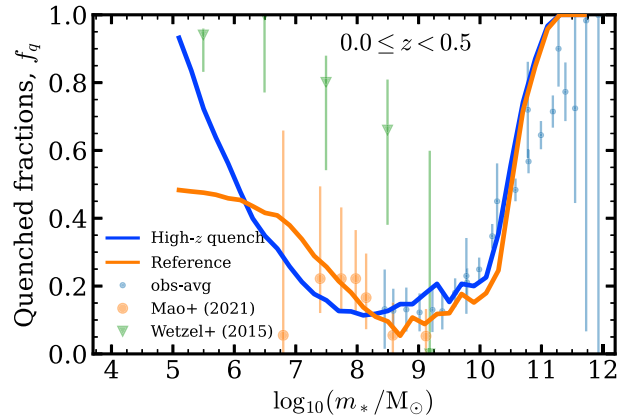


**Figure 10.** Quenched fractions as a function of mass at  $z = 0$  for our reference (orange line) and high- $z$  quenching model (blue line). Observed quenched fractions in the dwarf regime are indicated by orange circles and green triangles. The orange circles indicate results from the SAGA survey (Geha et al. 2017; Mao et al. 2021), and the green triangles show quenched fractions for Milky Way and Andromeda satellites (Wetzel, Tollerud & Weisz 2015). At higher masses, the observed average quenched fractions are indicated by blue points. A more complete view of the observable range at higher masses is illustrated in Fig. B4.

the local SMF still does not possess an average local SMF slope compared with simulated systems, but is still within the simulated range. In this case, the observed slope is steeper than the majority of simulated analogues. These deviations could indicate that assuming a global slope from local data is not adequate to constrain dwarf systems. To complicate the matter, halo masses for our simulated analogues tend to be higher than estimates for both Milky Way and

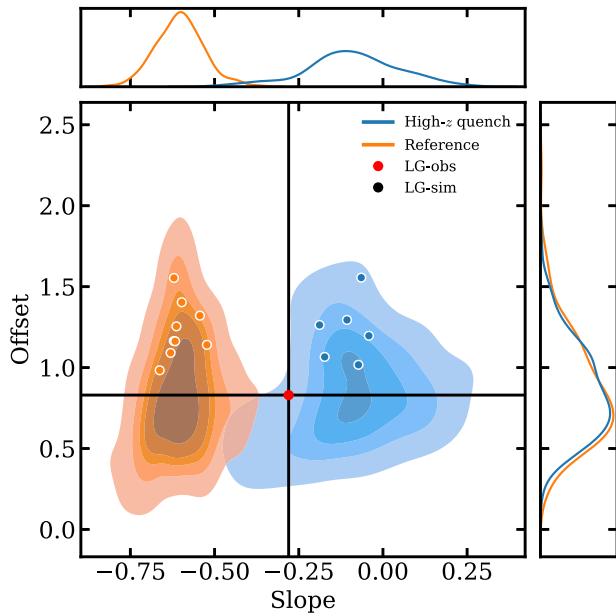


**Figure 11.** The relation between the locally measured density offset from the global averaged and the locally observed power law slope of the mass function for Milky Way like systems. Coloured contours show the distribution of these two properties based on the 2 Mpc spherical volume around simulated systems similar to the Milky Way, based only on stellar mass selection. Solid points indicate Milky Way analogues that also host a massive Andromeda like companion within 1 Mpc. The red marker shows the locally measured slope and offset based on the galaxies shown in Table A1 and illustrated by the observed mass function in Fig. 3.

Andromeda. The mismatch may or could indicate that the Local Group is indeed less dense than comparable counterparts and be subject to an accretion history that is not representative of haloes with comparable mass.

Finally, we have assumed that adopting a spherical volume is sufficient to describe the Local Group. Putman et al. (2021) instead propose a prolate Local Group surface to more accurately define group membership. It is unclear how our simplification might impact our goodness of fit or alter the demographics of Local Group analogues. This would be an interesting area for future work. Additionally, we have assumed that currently confirmed dwarf observations provide sample completeness down to  $\log_{10}(m^*/M_{\odot}) \sim 5$  (Tollerud et al. 2008). Other recent works suggest that the current sample of galaxies is incomplete due to selection bias and the local observed mass function ought to be higher (Loveday et al. 2015; Jethwa, Erkal & Belokurov 2018; Newton et al. 2018; Nadler et al. 2019, 2020; Drica-Wagner et al. 2020), which could also explain the dip in the SMF for  $\log_{10}(m^*/M_{\odot}) \lesssim 6.0$  (see Fig. 3). In testing, we found that allowing for a steeper mass function at low masses can negate the need for a high- $z$  quenching model and tend to prefer an earlier quenching with a lower  $M_q$ .

### 5.3 Other model options

The foundation for this work is the introduction of a basic model for high- $z$  quenching that has been implemented in order to match the characteristics of locally observed dwarf systems. This high- $z$  quenching model only shows that we can reproduce locally observed populations by imposing restrictions on star formation at high redshift in a manner consistent with expectations from reionization.

Limitations in our own implementation might restrict our ability to use this model to place direct constraints on the epoch of reionization. As implemented, this model does not and cannot accurately capture the richness of evolution imposed by a reionization process. In particular, all models we tested suppress galaxy formation via an instantaneous quenching mechanism, although there is evidence to suggest star formation may be periodic or even continue long after reionization (Geha et al. 2012; Skillman et al. 2017). The need for stars to form beyond reionization may explain why our models tend to favour such a late quenching scale  $a_q$ .

A key tenet of the empirical approach is to select the most simple model required to reproduce the observed data, only increasing the complexity when the data demands it. For the purposes of the analysis, in this work, we have instead adopted the slightly more complicated model in favour of its flexibility to constrain with the inclusion of future observables. There are, however, several sensible model options that could be explored if more information on the abundances and star formation histories of dwarfs becomes available.

#### 5.3.1 Augmented baryon conversion efficiency

Another reasonable approach to this problem would be to modify the standard baryon conversion efficiency with an additional term to further suppress the SFR in low mass haloes.

$$\epsilon(M) = 2\epsilon_N \left[ \left( \frac{M}{M_q} \right)^{-\alpha} + \left( \frac{M}{M_1} \right)^{-\beta} + \left( \frac{M}{M_1} \right)^{\gamma} \right]^{-1}. \quad (10)$$

While this approach is sensible and fits well within the current paradigm of the model, in testing, we found that SMF data alone was insufficient to appropriately constrain the larger number of free parameters of this variant. In particular, the redshift evolution of the terms  $\alpha$  and  $M_q$  is difficult to determine without more detailed measurements on the SFH of dwarfs. While the other models we test can quench and prevent star formation in haloes entirely, this method does not allow for empty haloes and does not introduce any explicit quenching mechanism.

#### 5.3.2 Quenching time-scales

Instead of shutting down star formation instantaneously, we could instead set a timer similar to the standard quenching treatment in EMERGE, allowing a more prolonged period for star formation after ‘reionization’. This would likely result in lower values for  $M_q$  and  $a_q$ . This option was not explored, but it may bring our high- $z$  quenching models in closer alignment with other models for reionization in cosmological simulations.

#### 5.3.3 Disc destruction

As noted in O’Leary et al. (2021), one of the lacking features of this model is the absence of proximity merging. Fig. 7 does not indicate that we have excessive satellites at small radii, at least not in the mass ranges we explore. However, Garrison-Kimmel et al. (2017) and Sawala et al. (2017) indicate that the presence of disc potential is significant for depletion of satellites in the inner halo. In our model, the suppression of the SMF is accomplished between the baryon conversion efficiency, the high- $z$  quenching and through tidal stripping. In reality, this is likely a more complex process that includes contributions from mergers or disruption due to the extended physical size of a host system. Here, we have not explored the relative

contributions of each of our model options on the abundance on dwarfs, but including additional mechanisms may alter our best fit model parameters. However, the parameters needed for these various mechanisms may be degenerate and locating observations that can independently constrain each parameter is problematic.

#### 5.4 Further analysis

Beyond the exploration of the SHMR, there are some additional studies that could be performed to better understand the lives and ultimate fate of galaxies in low mass haloes.

The bulk of this work has focused on the global statistics of dwarf galaxies. A deeper study of local satellite dwarfs may provide additional validation as these objects are most readily observable. In particular, a better understanding of when the Milky Way and Andromeda acquired their satellites may help relate the distribution and star formation histories of these systems. Understanding these correlations could help verify our predictions or constrain the model.

One direct consequence of our model is the existence of dark haloes. Other works explore this topic (Sawala et al. 2015, 2016a; Fitts et al. 2018) and establish an occupation fraction around  $\lesssim 10$  per cent for  $\log_{10}(M_h^{\text{peak}}/M_\odot) \lesssim 9$ . The observational confirmation of dark haloes would provide vital information for breaking parameter degeneracies, more accurately determining the impact of reionization physics on the SMHR and the broader relationship between galaxies and haloes. Further work in this area with EMERGE should include studies of dark haloes and their properties.

Furthermore, our models for high- $z$  quenching are rather *ad hoc* and may not accurately represent how this process should evolve with time. An alternative approach would be to utilize machine learning to inform a more appropriate parametrization. GALAXYNET (Moster et al. 2021) has already shown success for developing more accurate empirical prescriptions (see Section 2.2). Future improvements may make it possible to do the same with the high- $z$  quenching model. The primary development needed would be for the neural network to process complete merger trees instead of isolated snapshots this is necessary as the dwarf population is constrained by a low redshift observable that is driven by a high redshift process.

Finally, for this work our ability to fit the model with our chosen simulation was severely restricted by computational limitations of EMERGE. At present, EMERGE and other modern tree-based galaxy formation codes parallelize by distributing the input halo merger trees across cpu cores such that each individual tree is in shared memory and accessed by only a single task. For simulations in moderate volumes of moderate resolution, this is a completely adequate approach. When scaling these codes to more highly resolved simulations, there are often a handful of very massive trees that dominate the computation time leaving all other tasks idle while the massive trees are processed. This places a hard limitation on the rate that parameter space can be explored and, by extension, our ability to quantitatively compare models variations. Future studies of dwarf galaxy formation in EMERGE would benefit massively from refactoring the code to perform a more advance branch based parallelism that can allow for a more even distribution of the workload across many cores.

#### 5.5 Conclusions

Over the course of this work, we have developed an empirical model for galaxy formation with the goal of placing constraints on the stellar mass-halo mass relationship for galaxies down to  $\log_{10}(m^*/M_\odot) = 5$ . We achieve this goal by introducing an empirical quenching mechanism that approximates the effects of a reionization process.

This model is constrained by our extension of the global galaxy SMF using the mass function observed in the Local Group volume out to 2 Mpc.

While our model has been fit assuming a global mass function, we show that our simulated galaxy sample reproduces both the number density and radial distributions of satellites for the Milky Way and Andromeda. Additionally, our simulated galaxies are able to reproduce properties of observed systems beyond stellar mass. In particular, we find that for the  $z = 0$  sample, nearly 100 per cent of galaxies are quenched at  $\log_{10}(m^*/M_\odot) \sim 5$ . This is 50 per cent higher than a model that does not include high- $z$  quenching. Further, we show that introducing high- $z$  quenching produces a population of galaxies that better matches the star formation histories and formation time-scales of observed dwarf satellites.

We show that the SHMR can be extended as a power-law down to at least  $\log_{10}(M_h^{\text{peak}}/M_\odot) \approx 10$ . Models including high- $z$  quenching indicated substantially reduced scatter in peak halo mass at a fixed stellar mass and show that the elimination of high scatter galaxies in the tail of the distribution are the primary mechanism that flattens the SMF at low masses. Further inspection of the SHMR shows that there should be almost no galaxies down to  $\log_{10}(m^*/M_\odot) = 5$ , with a peak halo mass lower than  $\log_{10}(M_h^{\text{peak}}/M_\odot) \lesssim 9.0$ . This is consistent with our model implementations which predict quenching in haloes with  $\log_{10}(M_h^{\text{peak}}/M_\odot) \lesssim 9.3$  by  $z = 4$  (see Table 1)

Incorporating a model which suppresses star formation in low mass-high redshift haloes produces a population of galaxies that is consistent with observables in both the total number density and in the bulk SFH of galaxies. Our results indicate that as few as two additional free parameters are necessary to reproduce the number density of dwarf galaxies. However, we propose a more complex 3 parameter logistic model as the framework for model variations due to its adaptability.

#### ACKNOWLEDGEMENTS

We thank all authors who provide their data in electronic form. The cosmological simulations used in this work were partially carried out at the Odin Cluster at the Max Planck Computing and Data Facility and SuperMUC-NG in Garching. The authors gratefully acknowledge the Gauss Centre for Supercomputing e.V. ([www.gauss-centre.eu](http://www.gauss-centre.eu)) for funding this project by providing computing time on the GCS Supercomputer SuperMUC-NG at Leibniz Supercomputing Centre ([www.lrz.de](http://www.lrz.de)) via the project number pn72bu. The authors acknowledge the computing time provided by the cluster “rusty” of the Simons Foundation in New York City. UPS is supported by a Flatiron Research Fellowship (FRF) at the Center of Computational Astrophysics at the Flatiron Institute. The Flatiron Institute is supported by the Simons Foundation. Finally, we thank the developers of Astropy (Astropy Collaboration 2013, 2018), NumPy (van der Walt, Colbert & Varoquaux 2011), SciPy (Virtanen et al. 2020), Jupyter (Ragan-Kelley et al. 2014), Matplotlib (Hunter 2007), for their very useful free software. The Astrophysics Data Service (ADS) and arXiv preprint repository were used extensively in this work.

#### DATA AVAILABILITY

The data will be made available based on reasonable request to the corresponding author.

## REFERENCES

- Applebaum E., Brooks A. M., Christensen C. R., Munshi F., Quinn T. R., Shen S., Tremmel M., 2021, *ApJ*, 906, 96
- Astropy Collaboration, 2013, *A&A*, 558, A33
- Astropy Collaboration, 2018, *AJ*, 156, 123
- Beck A. M. et al., 2016, *MNRAS*, 455, 2110
- Behroozi P. S., Wechsler R. H., Wu H.-Y., 2013a, *ApJ*, 762, 109
- Behroozi P. S., Wechsler R. H., Wu H.-Y., Busha M. T., Klypin A. A., Primack J. R., 2013b, *ApJ*, 763, 18
- Behroozi P., Wechsler R. H., Hearin A. P., Conroy C., 2019, *MNRAS*, 488, 3143
- Bell E. F., de Jong R. S., 2001, *ApJ*, 550, 212
- Benitez-Llambay A., Fumagalli M., 2021, *ApJ*, 921, L9
- Bland-Hawthorn J., Gerhard O., 2016, *ARA&A*, 54, 529
- Bullock J. S., Kravtsov A. V., Weinberg D. H., 2000, *ApJ*, 539, 517
- Carlsten S. G., Greene J. E., Peter A. H. G., Beaton R. L., Greco J. P., 2020, *ApJ*, 908, 36
- Cole A. A., Weisz D. R., Dolphin A. E., Skillman E. D., McConnachie A. W., Brooks A. M., Leaman R., 2014, *ApJ*, 795, 54
- Cooray A., 2006, *MNRAS*, 365, 842
- Diaz J. D., Koposov S. E., Irwin M., Belokurov V., Evans N. W., 2014, *MNRAS*, 443, 1688
- Drlica-Wagner A. et al., 2020, *ApJ*, 893, 47
- Efstathiou G., Bond J. R., White S. D. M., 1992, *MNRAS*, 258, 1P
- Fattahi A., Navarro J. F., Frenk C. S., 2020, *MNRAS*, 493, 2596
- Fitts A. et al., 2018, *MNRAS*, 479, 319
- Gallart C. et al., 2015, *ApJ*, 811, L18
- Garrison-Kimmel S. et al., 2017, *MNRAS*, 471, 1709
- Garrison-Kimmel S. et al., 2019, *MNRAS*, 487, 1380
- Geha M., Blanton M. R., Yan R., Tinker J. L., 2012, *ApJ*, 757, 85
- Geha M. et al., 2017, *ApJ*, 847, 4
- Hahn O., Abel T., 2011, *MNRAS*, 415, 2101
- Hirano S., Hosokawa T., Yoshida N., Omukai K., Yorke H. W., 2015, *MNRAS*, 448, 568
- Hunter J. D., 2007, *Comput. Sci. Eng.*, 9, 90
- Jethwa P., Erkal D., Belokurov V., 2018, *MNRAS*, 473, 2060
- Klypin A., Kravtsov A. V., Valenzuela O., Prada F., 1999, *ApJ*, 522, 82
- Kravtsov A., Manwadkar V., 2022, *MNRAS*, 514, 2667
- Kuhlen M., Madau P., Krumholz M. R., 2013, *ApJ*, 776, 34
- Kulkarni M., Visbal E., Bryan G. L., 2021, *ApJ*, 917, 40
- Lewis A., Challinor A., Lasenby A., 2000, *ApJ*, 538, 473
- Loveday J. et al., 2015, *MNRAS*, 451, 1540
- McConnachie A. W., 2012, *AJ*, 144, 4
- Mao Y.-Y., Geha M., Wechsler R. H., Weiner B., Tollerud E. J., Nadler E. O., Kallivayalil N., 2021, *ApJ*, 907, 85
- Martin N. F., de Jong J. T. A., Rix H.-W., 2008, *ApJ*, 684, 1075
- Moore B., Ghigna S., Governato F., Lake G., Quinn T., Stadel J., Tozzi P., 1999, *ApJ*, 524, L19
- Moster B. P., Somerville R. S., Maulbetsch C., van den Bosch F. C., Macciò A. V., Naab T., Oser L., 2010, *ApJ*, 710, 903
- Moster B. P., Naab T., White S. D. M., 2018, *MNRAS*, 477, 1822
- Moster B. P., Naab T., Lindström M., O’Leary J. A., 2021, *MNRAS*, 507, 2115
- Munshi F., Brooks A., Applebaum E., Christensen C., Sligh J. P., Quinn T., 2021, *ApJ*, 923, 14
- Nadler E. O., Mao Y.-Y., Green G. M., Wechsler R. H., 2019, *ApJ*, 873, 34
- Nadler E. O. et al., 2020, *ApJ*, 893, 48
- Newton O., Cautun M., Jenkins A., Frenk C. S., Helly J. C., 2018, *MNRAS*, 479, 2853
- O’Leary J. A., Moster B. P., Naab T., Somerville R. S., 2021, *MNRAS*, 501, 3215
- Planck Collaboration, 2016, *A&A*, 594, A13
- Putman M. E., Zheng Y., Price-Whelan A. M., Grcevich J., Johnson A. C., Tollerud E., Peek J. E. G., 2021, *ApJ*, 913, 53
- Ragan-Kelley M., Perez F., Granger B., Kluyver T., Ivanov P., Frederic J., Bussonnier M., 2014, AGU Fall Meeting Abstracts, p. H44D
- Rey M. P., Starkeburg T. K., 2022, *MNRAS*, 510, 4208
- Rey M. P., Pontzen A., Agertz O., Orkney M. D. A., Read J. I., Rosdahl J., 2020, *MNRAS*, 497, 1508
- Ricotti M., Gnedin N. Y., Shull J. M., 2008, *ApJ*, 685, 21
- Sawala T. et al., 2015, *MNRAS*, 448, 2941
- Sawala T. et al., 2016a, *MNRAS*, 456, 85
- Sawala T. et al., 2016b, *MNRAS*, 457, 1931
- Sawala T., Pihajoki P., Johansson P. H., Frenk C. S., Navarro J. F., Oman K. A., White S. D. M., 2017, *MNRAS*, 467, 4383
- Schauer A. T. P., Glover S. C. O., Klessen R. S., Clark P., 2021, *MNRAS*, 507, 1775
- Sick J., Courteau S., Cuillandre J.-C., Dalcanton J., de Jong R., McDonald M., Simard D., Tully R. B., 2015, in Cappellari M., Courteau S., eds. *IAU Symp. 311, Galaxy Masses as Constraints of Formation Models*. p. 82
- Simon J. D., 2018, *ApJ*, 863, 89
- Skillman E. D. et al., 2017, *ApJ*, 837, 102
- Smercina A., Bell E. F., Price P. A., D’Souza R., Slater C. T., Bailin J., Monachesi A., Nidever D., 2018, *ApJ*, 863, 152
- Somerville R. S., 2002, *ApJ*, 572, L23
- Springel V., 2005, *MNRAS*, 364, 1105
- Thoul A. A., Weinberg D. H., 1996, *ApJ*, 465, 608
- Tollerud E. J., Bullock J. S., Strigari L. E., Willman B., 2008, *ApJ*, 688, 277
- van der Walt S., Colbert S. C., Varoquaux G., 2011, *Comput. Sci. Eng.*, 13, 22
- Virtanen P. et al., 2020, *Nature Methods*, 17, 261
- Wang Y., Nadler E. O., Mao Y.-Y., Adhikari S., Wechsler R. H., Behroozi P., 2021, *ApJ*, 915, 17
- Weisz D. R., Dolphin A. E., Skillman E. D., Holtzman J., Gilbert K. M., Dalcanton J. J., Williams B. F., 2014, *ApJ*, 789, 147
- Weisz D. R., Dolphin A. E., Skillman E. D., Holtzman J., Gilbert K. M., Dalcanton J. J., Williams B. F., 2015, *ApJ*, 804, 136
- Weisz D. R. et al., 2019, *ApJ*, 885, L8
- Wetzel A. R., Tollerud E. J., Weisz D. R., 2015, *ApJ*, 808, L27
- Woo J., Courteau S., Dekel A., 2008, *MNRAS*, 390, 1453

## APPENDIX A: OBSERVED DWARF DATA

The table in this section tabulates the dwarf catalogue data that was used to extend our model constraints to  $\log_{10}(m^*/M_{\odot}) \approx 5$ . The table additionally includes details on the distance of each system to the Milky Way and Andromeda (M31), as well as 90 per cent formation time-scales used for the comparisons in Section 4.4.

**Table A1.** Catalogue of Local Group dwarf galaxies and their properties used in this work. The reference column indicates the source for the  $\tau_{90}$  measurements.

Galaxy Name	$\log_{10}(m^*/M_{\odot})$	$D_{\odot}$ [kpc]	$D_{MW}$ [kpc]	$D_{M31}$ [kpc]	$\tau_{90}$ [Gyr]	Reference
Sagittariusd-Sph	7.526	27	19	787	$10.3^{+0.33}_{-1.82}$	Weisz et al. (2014)
LMC	9.380	51	50	807	-	-
SMC	8.867	64	61	807	-	-
UrsaMinor	5.748	76	78	754	$4.63^{+3.27}_{-1.60}$	Weisz et al. (2014)
Draco	5.681	82	82	748	$3.55^{+2.50}_{-1.52}$	Weisz et al. (2014)
Sculptor	6.459	86	86	761	$3.09^{+3.53}_{-1.29}$	Weisz et al. (2014)
Sextans(1)	5.709	95	98	841	-	-
Carina	5.920	106	108	838	$11.46^{+0.07}_{-1.49}$	Weisz et al. (2014)
Crater 2	5.408	118	116	886	-	-
Antlia 2	5.748	132	133	889	-	-
Fornax	7.483	139	141	768	$11.46^{+0.20}_{-0.27}$	Weisz et al. (2014)
Canes Venatici(1)	5.635	211	211	856	$5.38^{+2.01}_{-1.13}$	Weisz et al. (2014)
Leo 2	6.030	233	236	897	$7.29^{+0.63}_{-0.75}$	Weisz et al. (2014)
Leo 1	6.848	254	258	918	$12.02^{+0.06}_{-0.20}$	Weisz et al. (2014)
Leo T	5.350	409	414	982	$12.12^{+0.12}_{-0.06}$	Weisz et al. (2014)
Phoenix	6.091	415	415	864	$10.56^{+0.63}_{-1.03}$	Gallart et al. (2015)
NGC6822	8.204	459	452	894	-	-
Andromeda XVI	5.736	476	480	319	$7.88^{+0.56}_{-0.49}$	Skillman et al. (2017)
Andromeda XXIV	5.173	600	605	204	$8.4^{+3.1}_{-4.4}$	Weisz et al. (2019)
NGC185	8.037	617	621	184	-	-
Andromeda XV	5.885	625	630	175	$4.24^{+0.87}_{-3.13}$	Skillman et al. (2017)
Andromeda II	7.163	652	656	181	$7.39^{+0.60}_{-0.51}$	Skillman et al. (2017)
Andromeda XXVIII	5.526	661	661	365	$6.13^{+0.28}_{-1.75}$	Skillman et al. (2017)
Andromeda X	5.149	670	674	130	$7.3^{+2.1}_{-4.8}$	Weisz et al. (2019)
NGC147	7.997	676	680	139	-	-
Andromeda XXX	5.318	682	686	144	-	-
Andromeda XVII	5.547	728	732	66	$3.3^{+5.0}_{-2.1}$	Weisz et al. (2019)
Andromeda XXIX	5.459	731	734	187	$8.6^{+1.2}_{-2.2}$	Weisz et al. (2019)
Andromeda I	6.876	745	749	55	$6.29^{+0.67}_{-0.84}$	Skillman et al. (2017)
Andromeda III	6.204	748	752	73	$4.93^{+0.67}_{-1.47}$	Skillman et al. (2017)
IC1613	8.204	755	758	518	$11.46^{+0.63}_{-1.03}$	Gallart et al. (2015)
Cetus	6.651	755	756	678	$4.3^{+0.63}_{-1.03}$	Gallart et al. (2015)
Andromeda XXXI	6.817	759	760	262	-	-
Andromeda VII	7.408	762	765	217	-	-
Andromeda IX	5.380	766	770	39	$8.7^{+2.0}_{-1.8}$	Weisz et al. (2019)
LGS3	6.186	769	773	268	$7.82^{+0.63}_{-1.03}$	Gallart et al. (2015)
Andromeda XXIII	6.246	769	774	126	$8.7^{+2.8}_{-1.5}$	Weisz et al. (2019)
Andromeda XXXIII	6.283	773	779	348	-	-
Andromeda V	5.952	773	777	109	-	-
Andromeda XXXII	7.037	776	780	140	-	-
Andromeda VI	6.723	783	785	268	-	-
Andromeda XIV	5.584	794	798	161	$9.0^{+0.7}_{-5.2}$	Weisz et al. (2019)
IC10	8.139	794	798	252	-	-
Leo A	6.982	798	803	1197	$12.55^{+0.63}_{-1.03}$	Gallart et al. (2015)
M32	8.709	805	809	27	-	-
Andromeda XXV	6.037	813	817	90	$8.0^{+1.3}_{-2.6}$	Weisz et al. (2019)
Andromeda XIX	5.723	820	824	115	-	-
NGC205	8.723	824	828	46	-	-
Andromeda XXI	6.049	828	831	135	$8.0^{+2.5}_{-0.9}$	Weisz et al. (2019)
Andromeda XXVII	5.283	828	832	77	-	-
Tucana	5.952	887	883	1352	$4.11^{+0.63}_{-1.03}$	Gallart et al. (2015)
Pegasus-dIrr	7.024	920	921	474	-	-
WLM	7.838	933	933	835	-	-
Sagittarius-dIrr	6.748	1067	1059	1354	-	-
Aquarius	6.408	1072	1066	1170	$11.1^{+0.02}_{-0.04}$	Cole et al. (2014)
Andromeda XVIII	5.903	1213	1217	457	$9.2^{+2.1}_{-1.7}$	Weisz et al. (2019)
Antlia B	6.003	1294	1296	1963	-	-
NGC3109	8.085	1300	1301	1984	-	-
Antlia	6.318	1349	1350	2036	-	-
UGC4879	7.123	1361	1367	1394	-	-
Sextans B	7.920	1426	1429	1940	-	-
Sextans A	7.848	1432	1435	2024	-	-
Leo P	5.795	1622	1625	2048	-	-
KKR25	6.505	1923	1922	1869	-	-
ESO410-G005	6.748	1923	1922	1861	-	-
IC5152	8.350	1950	1945	2209	-	-

## APPENDIX B: MODEL VARIANTS

## B1 Model fits to observables

In this section, we show how each model variant agrees with the observable constraints of each model. The observables indicated in the figures in this section correspond to the actual data used during fitting. Fig. B1 shows how well each best fit model reproduces the observed comsic star formation rate density (CSFRD). In Fig. B2 we compar model predictions of the observed stellar mass function (SMF) in twelve redshift bins. Model predictions of the specific star formation rate (sSFR) across four stellar mass bins is shown Fig.

B3. Finally, Fig. B4 illustrates how each model quenched fractions compared with observables.

## B2 Model predictions for dwarfs

Here, we show the complete results of our analysis for the model variants we did not highlight in the main text. First, we show predictions on the stellar-to-halo mass relation (SHMR) for each model in Fig. B5. Satellite mass functions for each model are illustrated in Fig. B6. The predicted radial distribution of dwarf satellites is shown in Fig. B7. Lastly, Fig. B8 displays the 90 percent formation time scales under each model.

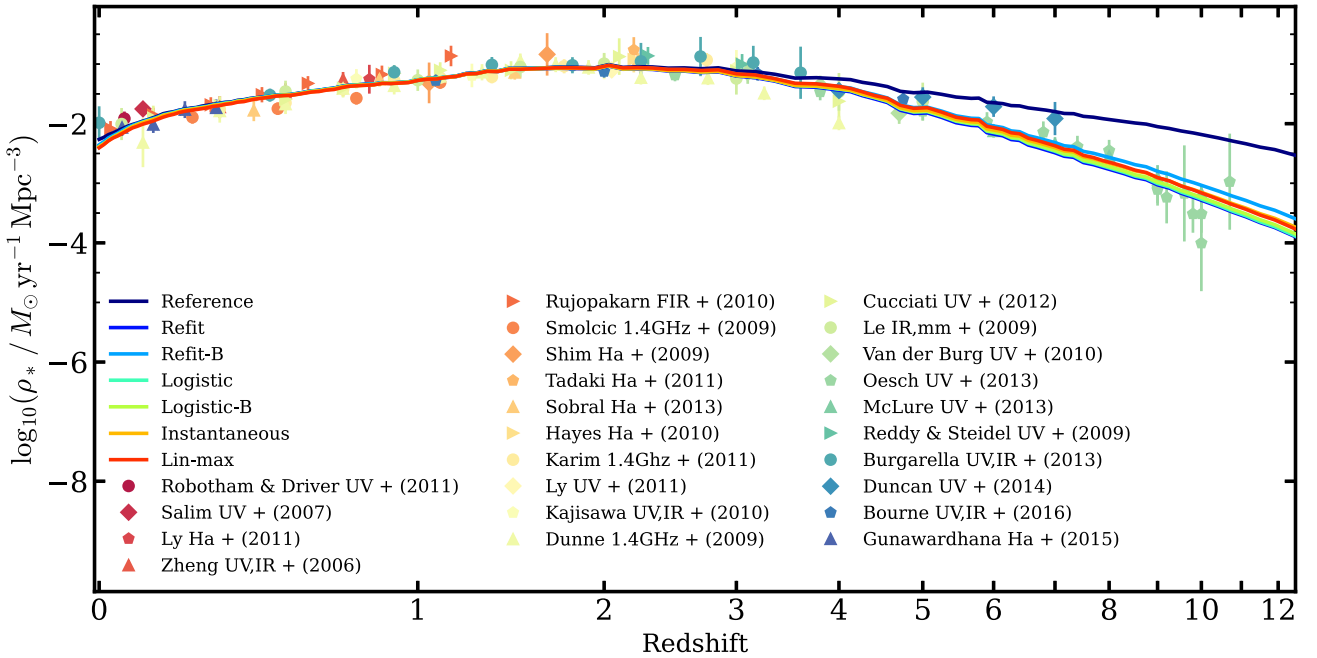
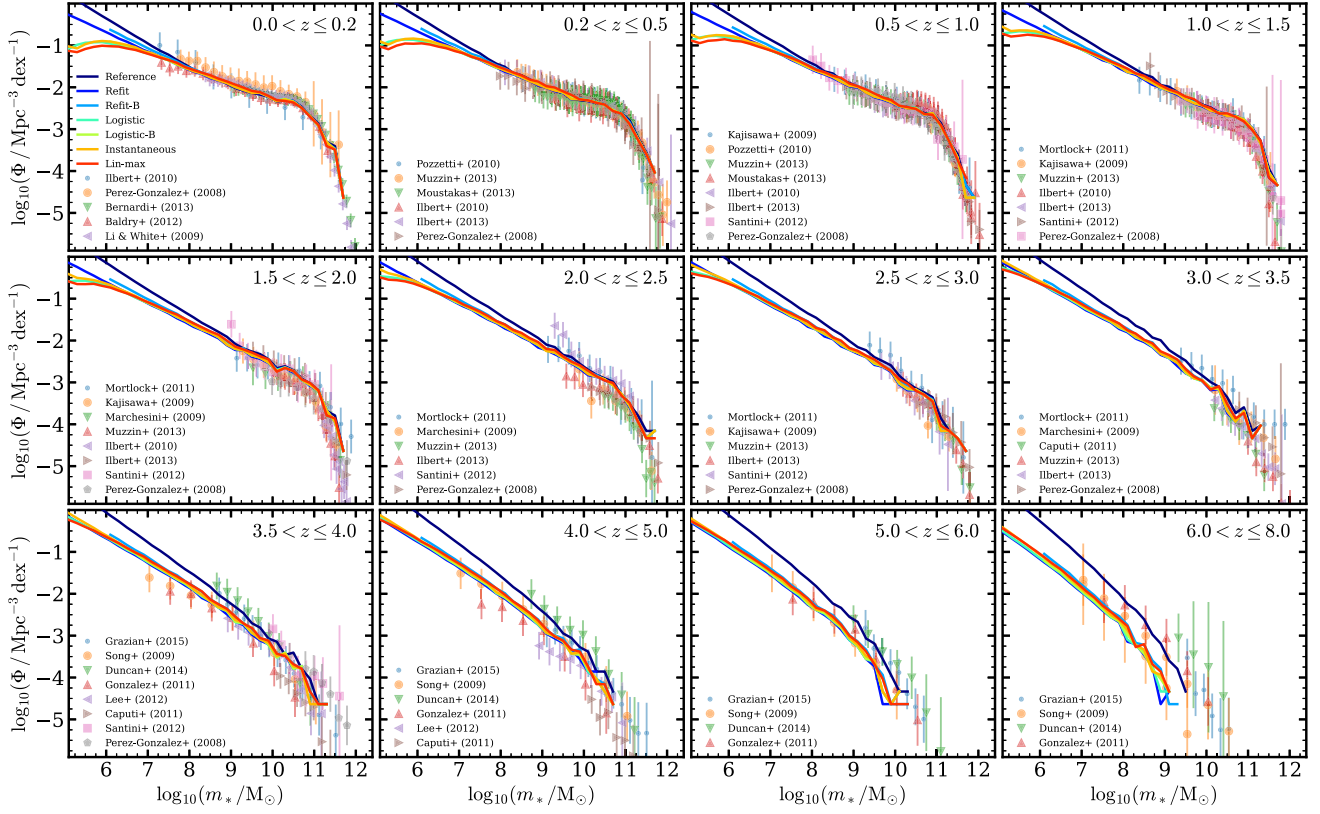
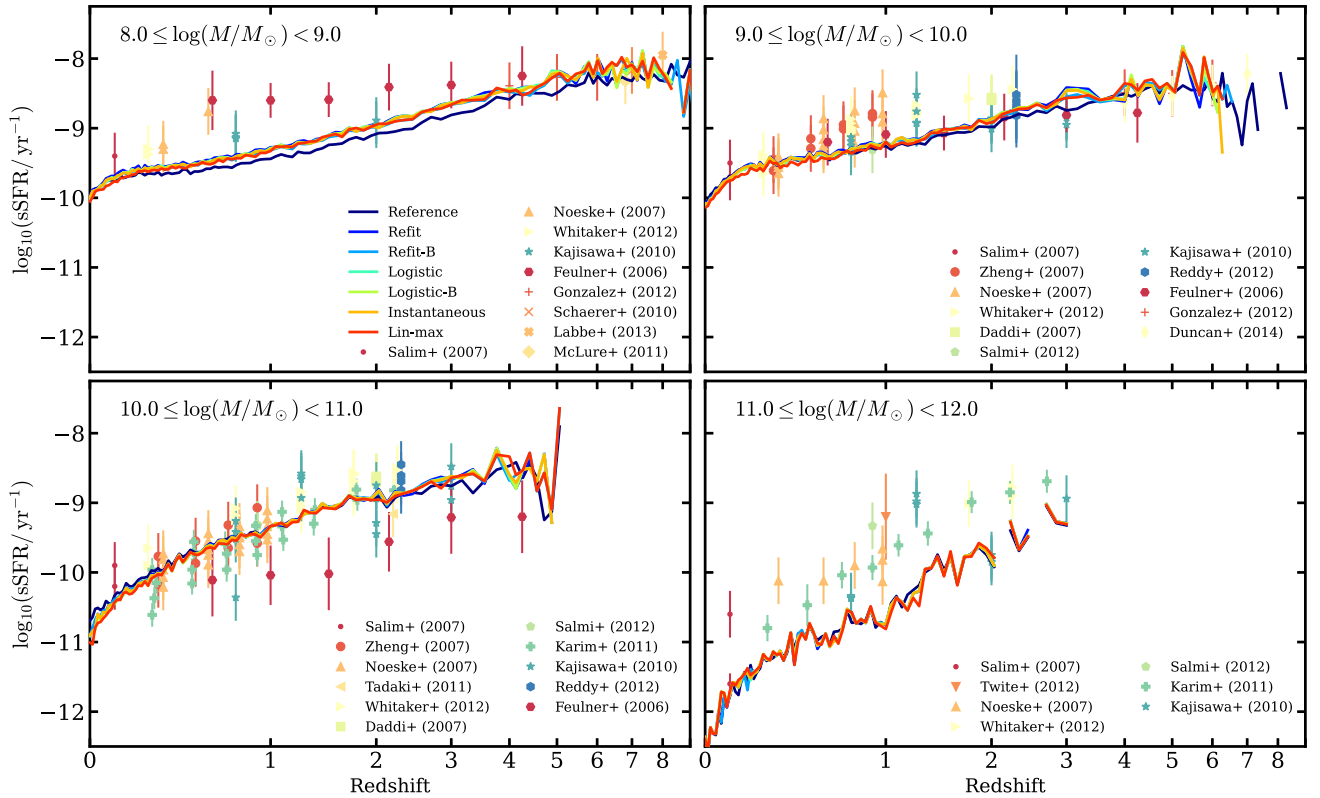


Figure B1. The model predicted cosmic star formation rate density compared to the input observables for each of our model variants.



**Figure B2.** The model predicted galaxy SMF compared to the input observables for each of our model variants.



**Figure B3.** The model predicted specific star formation rates compared to the input observables for each of our model variants.

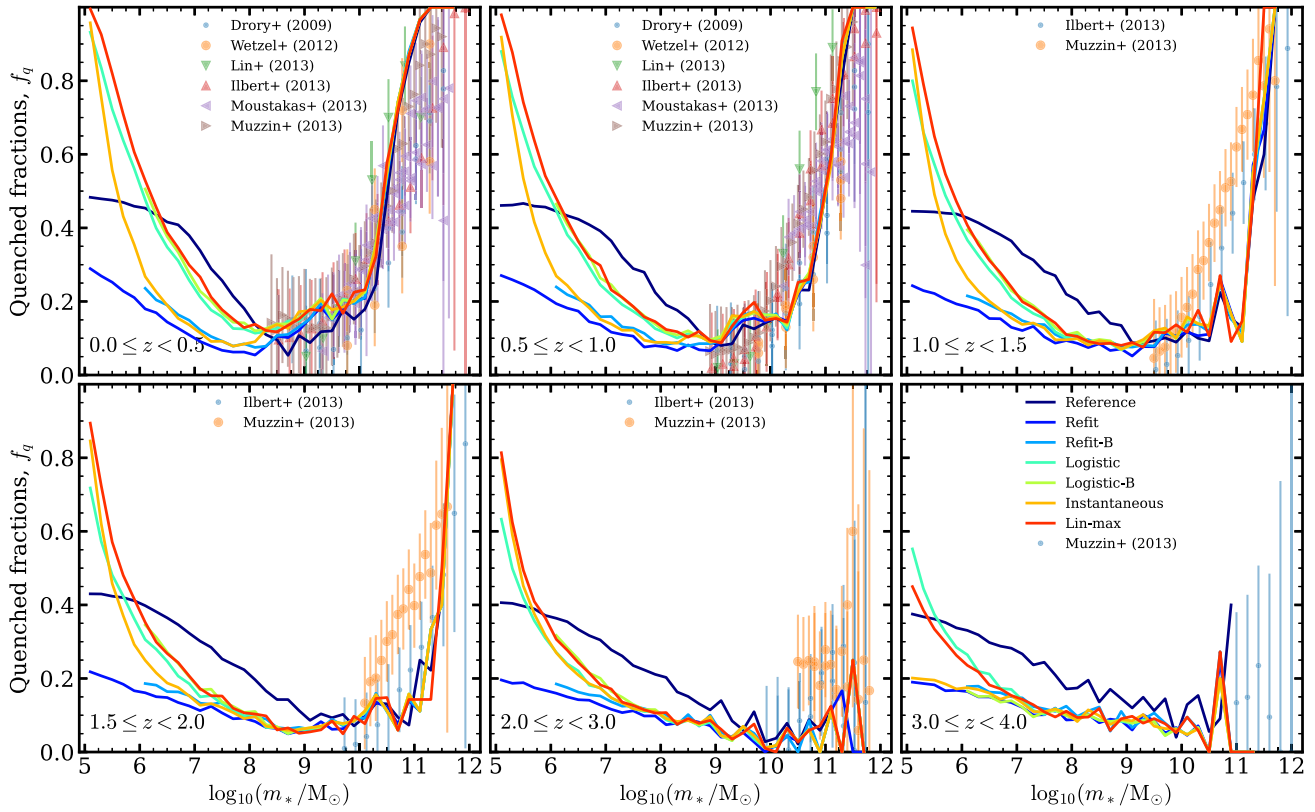


**Figure B4.** The model predicted quenched fractions compared to the input observables for each of our model variants.

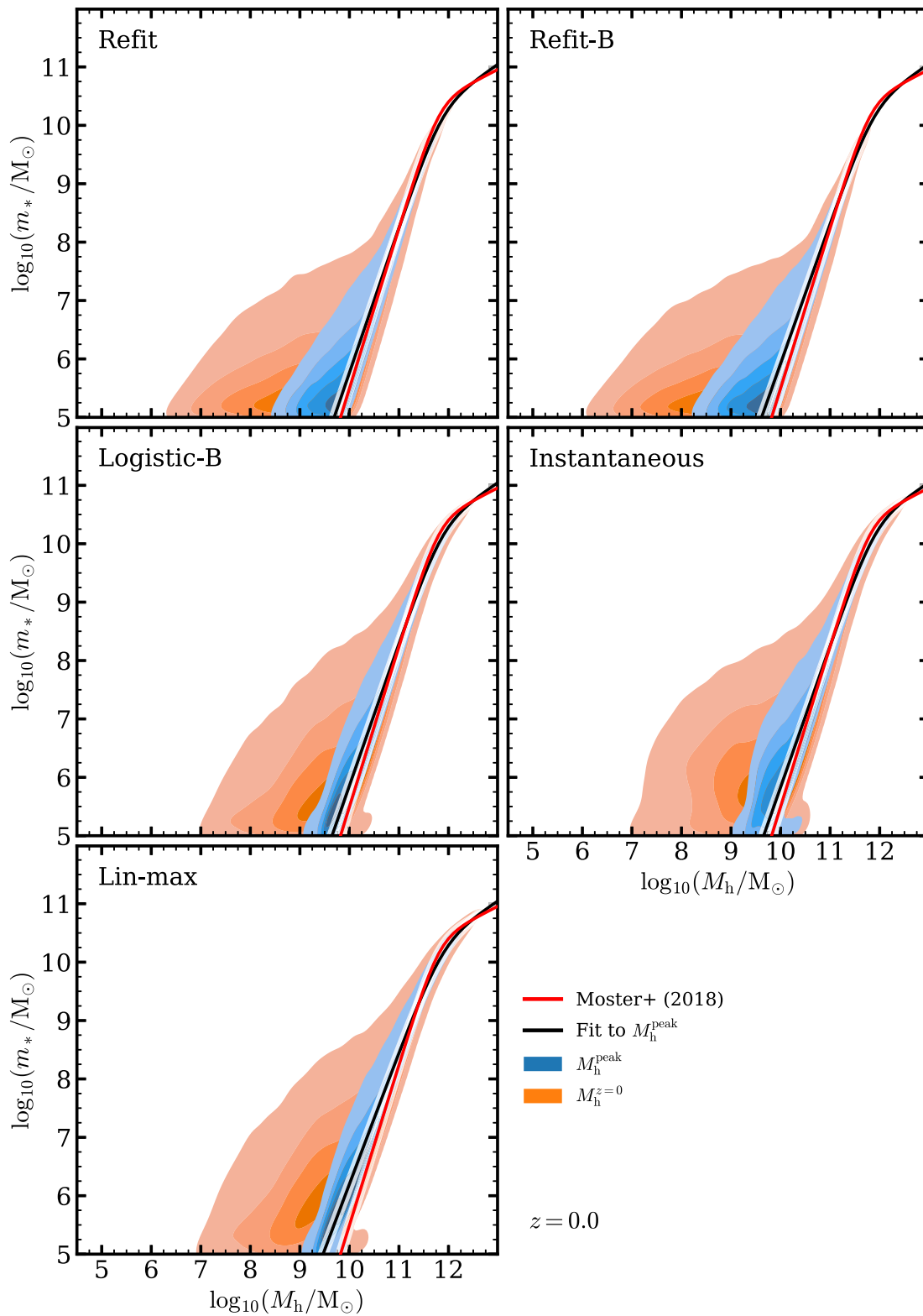


**Figure B5.** The predicted SHMR for each model variant.

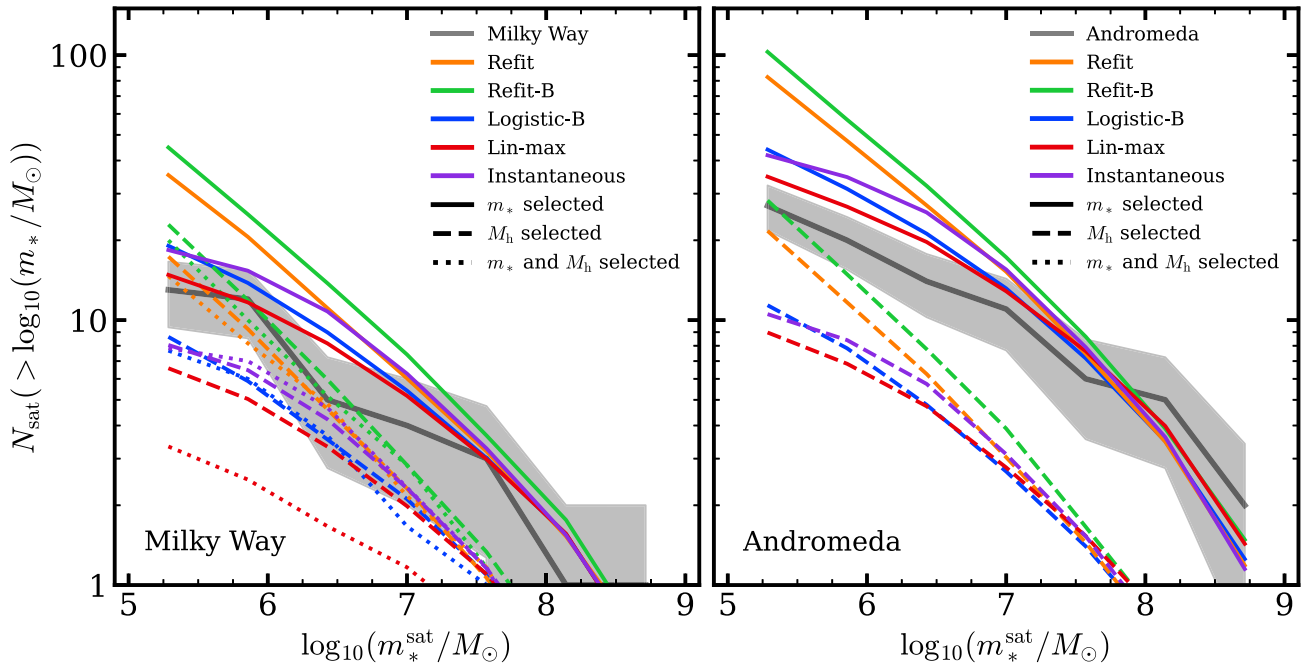


**Figure B6.** The predicted cumulative dwarf satellite mass function for each model variant.

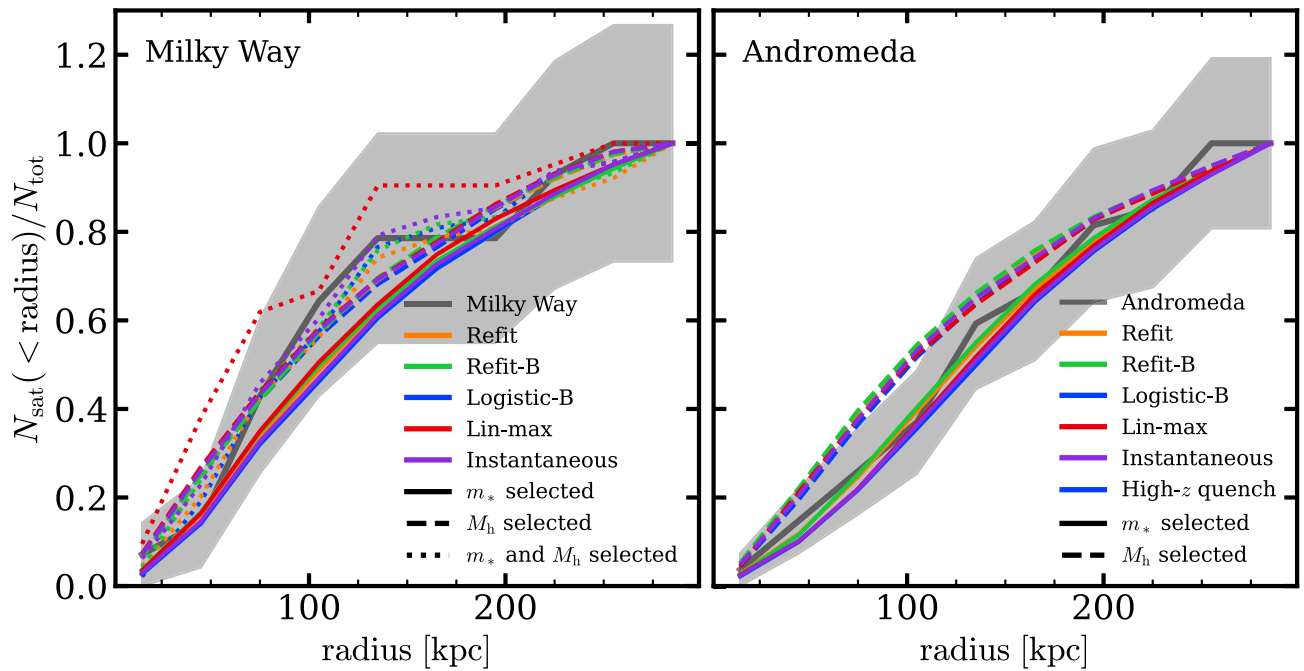


**Figure B7.** The predicted cumulative dwarf satellite radial distribution for each model variant.

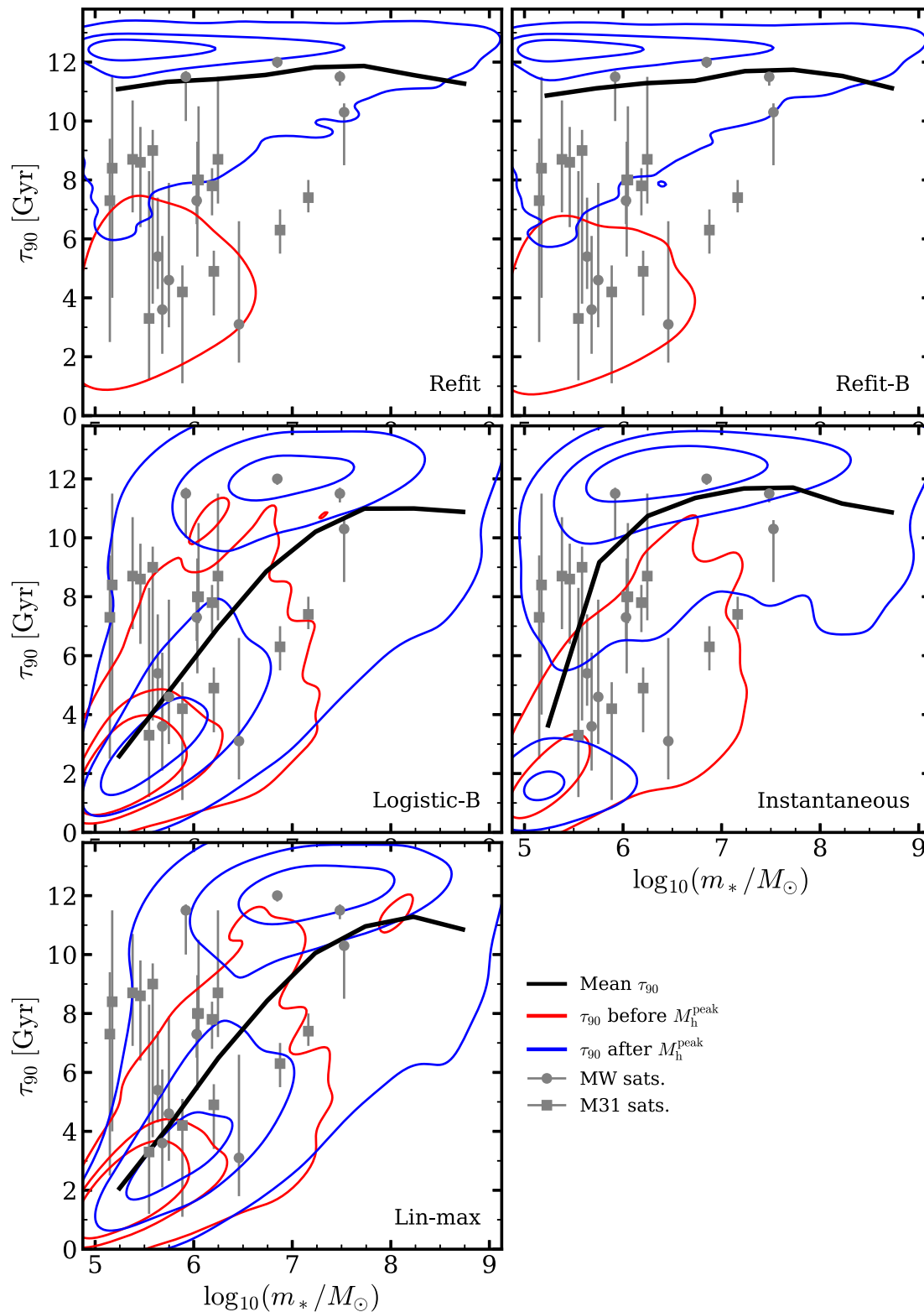


**Figure B8.** The predicted 90 percent formation time-scale for each model variant.

This paper has been typeset from a  $\text{\TeX}/\text{\LaTeX}$  file prepared by the author.